Peter Kratochwill, BSc.
Mat.No. 01430673

Developing Density of States Techniques for Finite Density Lattice QCD

Master's Thesis
to achieve the university degree of
Master of Science (MSc.)
Master's degree programme: Physics

Graz University
&
Graz University of Technology

Supervisor: Univ.-Prof. Dr.rer.nat. Christof Gattringer
Institute of Physics

Graz, May 2021

Abstract (English Version)

One of the four known fundamental forces of physics is the strong interaction, which in the Standard Model of Particle Physics is included by Quantum Chromodynamics (QCD). This theory aims to describe the interaction between quarks and gluons and the formation of baryonic matter. For experimental tests of the strong interaction at high temperatures and high densities heavy-ion collisions are performed in particle colliders. To describe the processes involved in these experiments theoretically, it is vital to understand QCD at a non-perturbative level. Lattice QCD has proved itself to be an efficient approach for high temperatures, but suffers from a numerical difficulty for finite densities, called the sign problem, which renders Monte Carlo methods inapplicable. In this thesis we investigate a numerical method which rewrites QCD in terms of a canonical density of states (CDoS) to avoid the sign problem so that standard implementations are possible again. Special attention was paid to the evaluation of the Dirac determinant by expressing the fermion degrees of freedom in terms of multi-bosons. The CDoS technique was tested for a simplified theory as well as for full QCD in 2 dimensions. Since the results obtained for the latter are inconclusive, more advanced Monte Carlo methods are required for future implementations of this approach.

Abstract (Deutsche Fassung)

Eine der der vier bekannten fundamentalen Kräfte der Physik ist die Starke Wechselwirkung, welche im Standardmodell der Teilchenphysik mit Hilfe der Quantenchromodynamik (QCD) formuliert wird. Das Ziel dieser Theorie ist die Beschreibung der Wechselwirkung zwischen Quarks und Gluonen, als auch die Entstehung aller baryonischer Materie. Als experimentelle Tests zur Starken Wechselwirkung bei hohen Temperaturen und hohen Dichten werden Schwerionen-Kollisionsexperimente mit Teilchenbeschleunigern durchgeführt. Um alle Vorgänge in diesen Experimenten beschreiben zu können ist ein detailliertes, nicht perturbatives Verständnis von QCD von Nöten. Für Hochtemperatur-Prozesse hat sich die Gitter-QCD als effizient bewiesen. Vorgänge bei endlichen Dichten sind hiermit aber aufgrund des sogenannten Vorzeichenproblems nicht mit Monte-Carlo Methoden berechenbar. In dieser Arbeit untersuchen wir einen numerischen Ansatz, welcher die Theorie der QCD mit Hilfe einer kanonische Zustandsdichte (CDoS) formuliert. Auf die Weise kann das Vorzeichenproblem umgangen und numerische Standardmethoden wieder angewendet werden. Besonderes Augenmerk wurde auf die Dirac-Determinante gelegt, die berechnet wurde indem die fermionischen Freiheitsgrade mittels Multi-Bosonen approximiert wurden. Die CDoS Methode wurde für eine vereinfachte Theorie aber auch für die vollständige QCD in 2 Dimensionen getestet. Da letzteres keine schlüssigen Ergebnisse lieferte, sind für zukünftige Anwendung dieser Methode fortschrittlichere Monte-Carlo Techniken notwendig.

Table of Contents

1. Introduction

Modern theoretical particle physics knows four fundamental forces with which all known interactions between particles can be described. Three of these forces, namely the electromagnetic, the weak and the strong interaction, as well as all known elementary particles are described in a theory which is called the *Standard Model of Particle Physics*. This theory has proven to be a suitable description for many aspects of fundamental physics, since its predictions are in very good agreement with experimental results [1]. Despite its many successes, the Standard Model is still not a complete theory, in the sense that it only contains three of the four known forces, because up to this date it has not been possible to incorporate gravitation into this theory.

In this thesis we will focus only on one of the three forces in the Standard Model, namely the strong interaction, which is responsible for forming the baryonic matter everything around us is made of. I.e. it holds together the quarks to form protons and neutrons, and on a larger scale it also holds together protons and neutrons to form atomic nuclei. The theory describing this interaction is called *Quantum Chromodynamics*, or QCD for short, which is a quantum field theory. We will use a special regularization of this quantum field by discretizing the continuous spacetime to an Euclidean lattice. This mathematical description of the quantum fields is called *Lattice Field Theory*.

One of the standard methods for numerical calculations in lattice field theories are Monte Carlo simulations. But in this work we will look at the behavior of the strong interaction for finite densities, which is to say for finite chemical potential. This gives rise to a numerical difficulty which is called the *sign problem* or the *complex action problem*, which prohibits the direct use of Monte Carlo methods. The main goal of this thesis is to test a numerical technique where the theory is rewritten in terms of a *Density of States*. This way the complex action problem can be overcome which makes Monte Carlo simulations accessible again.

The structure of this thesis will be as follows. At first, a very short overview of QCD and its lattice representation are given, where also the emergence of the sign problem is discussed. Following that, in the third chapter, the theoretical description of the density of states approach is given and the ansatz for its numerical calculation is explained. In the subsequent two chapters a numerical method is introduced which will be a very important tool for the implementation of the density of states method. Its applicability is also discussed and the method is tested by calculating simple observables. After that, a first implementation of the density of states method is presented for the free theory, where the results may still be compared with analytic the solutions. In the 7th chapter the Monte Carlo implementation of the full theory is explained and the obtained results, as well as possible improvements for the numerical implementation, are discussed.

The thesis is closed with a summary of the whole work and a short outlook for future applications of this density of states method.

2. QCD on the Lattice and the Sign Problem

In this chapter we give a very short overview of the basic ideas of Quantum Chromodynamics in general and then we will go into a little more detail when discussing the lattice description of the theory. We want to stress, though, that the purpose of this chapter is just to introduce the most important formulas used in this thesis. Therefore, derivations and proofs are for the most part not carried out here. In the third section of this chapter we will explain the origin of the so called sign problem, which is the main focus point of this work. Lastly, we will talk about some conventions needed and also fix some parameters which will then stay unchanged for the rest of the thesis.

2.1. Quantum Chromodynamics

The mathematical language in which the Standard Model of Particle Physics is formulated is called Quantum Field Theory. This ansatz combines the probabilistic and discretized nature at very small scales, as it is described in Quantum Mechanics, with Einstein's theory of special relativity. In this description particles are not considered to be fundamental objects. Instead, every kind of particle has an underlying field associated with it which spans over all of space and time. The quantized excitations of these fields can then be interpreted to be the particles we can measure and study in the laboratory.

As we already briefly discussed in the introduction, the part of the Standard Model we are interested in for this thesis is Quantum Chromodynamics, describing the strong interaction. This theory describes the fundamental interactions between the fermionic *quarks* and the bosonic *gluons*. Conceptually, QCD is similar to Quantum Electrodynamics (QED). In QED there exists just one charge, called the electric charge. Particles like the electron, for example, are carriers of that charge and they can interact with other electrically charged particles via the exchange of photons, the mediators of electromagnetism. QCD generalizes this idea. For strong interaction, there are three possible charges a particle can carry. These charges are called *color*. As for QED there are particles which mediate the interactions and these are the previously mentioned gluons. The important difference between these two theories is now that gluons themselves carry charge, which means they can interact with each other. This is not possible for the charge-neutral photons in QED. These additional possible interactions make the description of chromodynamics much more complicated and give also rise to interesting new properties.

One of these phenomenons which arises due to the self interactions of the gluons is called the *confinement of quarks*. This describes the fact that it is not possible to detect single, unbound quarks. All experimental evidence for quarks are as a part of compos-

ite particles[1], bound states of the strong interaction, called hadrons. These composite particles (baryons and mesons) are always color-neutral. Since confinement is a property which manifests itself only for large separations of quarks, it cannot be described by perturbation theory. So a rigorous theoretical description of confinement can only be achieved via non-perturbative approaches to Quantum Chromodynamics.

Of course, besides the general description of how quarks and gluons interact to form composite particles like baryons and mesons, it is also of interest to see how the theory behaves in more extreme conditions like for high temperatures or for high densities. Such conditions arise for example here on earth in particle colliders. So in order to be able to get an accurate understanding of the processes happening in these experiments and also in order to be able to interpret the measurements accurately it is of vital importance to study and understand the theory in these extreme circumstances.

Additionally, understanding QCD in these exceptional conditions does not only help to describe the smallest building blocks of our universe, but also to explain much larger, macroscopic objects: neutron stars. These remnants of supermassive stars are objects mainly made of neutrons with extremely high densities. This shows that, although QCD is a theory that aims to describe the smallest known objects, it is also a very important tool for our understanding of astrophysical objects found in our universe and is even needed to get an accurate understanding of cosmology.

So as a whole it can be said that it is of great importance to achieve a good description of QCD at high temperatures and high densities. In this work, we will use a non-perturbative description of QCD, called lattice field theory, which is well suited for numerical simulations. In this representation, however, the introduction of non-zero densities gives rise to difficulties regarding the numerical calculations. The main focus point of this thesis will be to circumvent these problems by rewriting the theory such that standard numerical methods are applicable again.

2.2. QCD on the Lattice

In this section, we want to give a short overview of the lattice description of QCD. It is important to note here that the derivation of the formulas is not part of this work. The aim is just to introduce the reader to the most important formulas needed and also to present the convention of notation used in this thesis. For an easy to understand introduction into the field of Quantum Chromodynamics on the lattice the reader is referred to [2].

The basic idea of lattice field theory is to discretize the continuous spacetime of quantum field theory to a finite Euclidean lattice. To set up this discretization we replace

[1] An exception are very high temperatures where QCD undergoes the so-called *deconfinement transition* and the quarks become liberated.

the d-dimensional spacetime vector $x^T = \{x_1, \ldots, x_d\}$ (^{T} denoting transposition) by a discretized vector,

$$x \to an. \tag{1}$$

Here, n is a vector of integer values labeling all the lattice sites and a is called the *lattice constant*, which carries the units of length and represents the physical distance between two lattice points. Since a is a scalar we have the same distance in all directions. The lattice Λ can then be defined as the set of all lattice sites via

$$\Lambda = \left\{ n \mid n^T = (n_1, \ldots, n_d)\,;\ n_\nu = 0, \ldots, N_\nu - 1;\ \nu = 1, \ldots, d \right\}, \tag{2}$$

where N_ν gives the number of lattice points in direction ν.

At this point it is necessary to mention some conceptual and notational differences between the continuous and the lattice description of the spacetime. For the continuous spacetime the Minkowskian metric is used, whereas our lattice is Euclidean. This means that there is no need to distinguish between upper and lower spacetime indices when dealing with the lattice formulation. Additionally, in the Minkowski space usually the zero-th component of a vector is the time component. For our Euclidean lattice description, however, we will use the convention that the time component is the d-th entry of a vector.

Now that we know how the lattice looks like, we can proceed by describing how the fields which live on the spacetime are influenced by this change of viewpoint. For fermions, which are described by Grassmann fields to incorporate the Fermi statistics, this implies now that they only have Grassmann degrees of freedom on the lattice sites. These will be denoted as $\psi(x) \to \psi(an) =: \psi(n)$. Here it is common practice to omit the lattice constant in the argument. For the gauge fields describing the gluons the change to the lattice formulation has somewhat more subtle consequences compared to the fermion fields. The gluons, which are in the continuous spacetime elements of the algebra su(3), are represented on the lattice by elements of the corresponding group SU(3), denoted as $A_\nu(x) \to U_\nu(an) =: U_\nu(n)$, where again a is suppressed in the argument. The $U_\nu(n)$ are called *gauge links* and since they carry a directional Lorentz index ν they live on the edges of the lattice and connect the two sites an and $an + a\hat{\nu}$. These matrices can therefore describe the interaction between fermions on neighboring lattice sites. Also, it is important to mention that the fields actually carry additional indices. The gauge links, being SU(3) matrices, carry two color indices and the fermion fields carry one color as well as one Dirac index. These we will usually not write down explicitly but use matrix/vector notation, as was also done above.

After defining the lattice spacetime and introducing the fields needed for QCD, it is important to mention how observables can be calculated. In quantum field theory in

general, this can be done via the path integral formulation. The expressions for vacuum expectation values then have a very similar appearance to that of expectation values in statistical mechanics and are given by

$$\langle \mathcal{O} \rangle = \frac{1}{Z} \int \mathcal{D}[\phi]\, e^{-S[\phi]} \mathcal{O}[\phi]. \tag{3}$$

The quantity in the denominator is called the partition function and can be expressed as

$$Z = \int \mathcal{D}[\phi]\, e^{-S[\phi]}. \tag{4}$$

The variable ϕ here is understood to represent all fields of the theory we want to study.

The measure of integration for a path integral is given in a way such that it integrates over all possible configuration of the fields ϕ. Formally, this can be achieved by performing an integration over the whole domain of the fields at every spacetime position. For a continuous theory, however, this implies an uncountable set of integrations, which cannot be rigorously defined [3]. For the discretized ansatz of lattice field theory, on the other hand, the measure can be given explicitly as a product of measures at every lattice site. So the path integral measure can be written as

$$\int \mathcal{D}[\phi] = \prod_{n \in \Lambda} \int \mathrm{d}\phi(n). \tag{5}$$

With this the partition function can be understood as being a weighted high dimensional integral over all possible configurations of the fields, where in quantum field theories the weight factor e^{-S} is called the Boltzmann factor, and $S\,[\phi]$ is the Euclidean action of the theory.

If we now use this path integral formulation to calculate observables of QCD, we have to perform integrations over all degrees of freedom. This means we have an integration over the gauge links U as well as the Grassmann fields ψ and $\overline{\psi}$ [2]. Therefore, the vacuum expectation value of some observable $\mathcal{O}$ is given by

$$\langle \mathcal{O} \rangle = \frac{1}{Z} \int \mathcal{D}[U]\, e^{-S_G[U]} \int \mathcal{D}\big[\,\overline{\psi}, \psi\big]\, e^{-S_F[\overline{\psi},\psi,U]} \mathcal{O}[\overline{\psi}, \psi, U], \tag{6}$$

where the expression for the partition function is

$$Z = \int \mathcal{D}[U]\, e^{-S_G[U]} \int \mathcal{D}\big[\,\overline{\psi}, \psi\big]\, e^{-S_F[\overline{\psi},\psi,U]}. \tag{7}$$

Here we already separated the action S into the gauge field action $S_G[U]$ and the fermion

[2] In the operator formulation ψ and $\overline{\psi}$ are related to one another, but in the path integral approach we treat them as separate and independent fields.

action $S_F[\overline{\psi}, \psi, U]$. The measure of the fermions is given by a product of integral measures for Grassmann variables:

$$\int \mathcal{D}[\,\overline{\psi}, \psi] = \prod_{n \in \Lambda} \int \mathrm{d}\overline{\psi}(n) \mathrm{d}\psi(n). \tag{8}$$

The measure for the gauge links can be expressed as

$$\int \mathcal{D}[U] = \prod_{n \in \Lambda} \prod_{\nu=1}^{d} \int \mathrm{d}U_\nu(n), \tag{9}$$

where we now not only have a product over all lattice points n, but also have to include all possible directions ν. This is due to the fact that the gauge links live on the edges of the lattice. The $\mathrm{d}U_\nu(n)$ are called Haar measures, which describe an integration over the group manifold of the SU(3) valued matrices $U_\nu(n)$.

Now we turn to discuss the weight factors of the integration. First, we will look at the gauge field action S_G where we use the Wilson gauge action first introduced by Wilson in 1974 [4]. It can be expressed as

$$S_G[U] = \frac{\beta}{3} \sum_{n \in \Lambda} \sum_{\nu < \rho} \mathrm{Re}\left[\mathrm{tr}\left\{\mathbb{1} - U_{\nu\rho}(n)\right\}\right], \tag{10}$$

$$U_{\nu\rho}(n) = U_\nu(n) U_\rho(n + \hat{\nu}) U_\nu^\dagger(n + \hat{\rho}) U_\rho^\dagger(n). \tag{11}$$

The quantities $U_{\nu\rho}(n)$ are called plaquettes and represent the smallest possible closed loops of gauge links. $\mathbb{1}$ denotes the three by three identity matrix for the color space. With the two sums all plaquettes are added up, where the restriction $\nu < \rho$ ensures that only one orientation of the plaquettes is counted. The prefactor β is called the inverse gauge coupling. It can be shown that in the limit of a vanishing lattice constant $a \to 0$ and the substitution $\beta = 6/g^2$ the action in Eq. (10) yields the correct expression for the continuum gauge action of QCD, with g being the gauge coupling in the continuum where it describes the coupling strength of the gauge fields to the fermions.

In the second weight factor of Eq. (7) is S_F, the so-called fermion action, which describes the quarks and their interaction with the gauge links U. It is a bilinear functional of the fermions $\overline{\psi}$ and ψ and can be expressed in the following way

$$S_F\left[\overline{\psi}, \psi, U\right] = a^d \sum_{n,m \in \Lambda} \overline{\psi}(n) D\left(n|m\right) \psi(m), \tag{12}$$

$$D\left(n|m\right)_{\substack{\alpha\beta\\ab}} = \left(m + \frac{d}{a}\right)\delta_{\alpha\beta}\delta_{ab}\delta_{nm} - \frac{1}{2a}\sum_{\nu=1}^{d}\Big\{\left[\mathbb{1} - \gamma_\nu\right]_{\alpha\beta} U_\nu(n)_{ab}\delta_{n+\hat{\nu},m} + \left[\mathbb{1} + \gamma_\nu\right]_{\alpha\beta} U_\nu^\dagger(n-\hat{\nu})_{ab}\delta_{n-\hat{\nu},m}\Big\}. \quad (13)$$

Here we have used matrix/vector notation for color and Dirac space in Eq. (12), but wrote down all the indices explicitly in Eq. (13), where the Greek letters are indices in Dirac space and the Latin letters indices in the color space. Here $\mathbb{1}$ stands for the unit matrix in Dirac space.

Writing the fermion action as in Eq. (12) makes the bilinearity of S_F obvious and simultaneously defines the quantity $D(n|m)$, which is called the *lattice Dirac operator* or, more fittingly, *lattice Dirac matrix*, and will be of major importance in this work. This quantity obviously depends on the gauge links U, which are not displayed as an argument for notational convenience at this point. The matrices γ_ν are the Euclidean gamma matrices. Their explicit form will be given later in this chapter when the spacetime dimension d is fixed. The quantities δ_{xy} are Kronecker deltas. Their value is equal to one if the two indices are identical and zero otherwise. Also, as usual, m denotes the mass of the fermion, which is here of course not to be confused with the lattice index of the same name.

What we also want to mention is the reason for the additional mass term $\frac{d}{a}$. This is a necessary alteration in the lattice formulation to overcome the so-called *doubling problem* which arises due to the discretization. Also the two $\mathbb{1}$ in the sum are part of this correction. Altogether these additional parts are called the *Wilson term*. Important is that when calculating the continuum limit of the fermion action, $a \to 0$, the Wilson term decouples from the theory and the correct expressions for the mass and the fermion-gluon interactions are achieved.

In this thesis, although, we will work with a slightly different representation of the Dirac operator than the one stated in Eq. (13). With a simple rescaling of the fermionic fields by $\psi \to \sqrt{m - \frac{a}{d}}\psi$ and $\overline{\psi} \to \sqrt{m - \frac{a}{d}}\,\overline{\psi}$ the Dirac operator changes to

$$D(n|m) = \mathbb{1} - \kappa H(n|m), \quad \text{with} \quad \kappa = \frac{1}{2\left(am + d\right)}, \quad (14)$$

$$H(n|m)_{\substack{\alpha\beta\\ab}} = \sum_{\nu=1}^{d}\Big\{\left[\mathbb{1} - \gamma_\nu\right]_{\alpha\beta} U_\nu(n)_{ab}\delta_{n+\hat{\nu},m} + \left[\mathbb{1} + \gamma_\nu\right]_{\alpha\beta} U_\nu^\dagger(n-\hat{\nu})_{ab}\delta_{n-\hat{\nu},m}\Big\}. \quad (15)$$

The quantity $H(n|m)$ defined this way is called the *hopping matrix* since it includes all nearest neighbor interactions of quarks and gluons. The scalar κ is accordingly called the *hopping parameter* and gives the mass dependence. The first term for the Dirac operator in Eq. (14) is given by an identity matrix in all spaces (position, Dirac and color space). We will discuss this representation in a little more detail in the next section when we

introduce the chemical potential.

Before we can turn to discussing the chemical potential, however, there is still an important relation regarding the numerical implementation of Eq. (6) which needs to be addressed. Due to the fact that the fermion action S_F is a bilinear functional, the integration over the fermion degrees of freedom has the form of a Gaussian Grassmann integral. Using this fact, the integration over the Grassmann fields in Eq. (7) can be calculated to be

$$Z_F = \int \mathcal{D}\big[\overline{\psi}, \psi\big]\, e^{-\overline{\psi} D \psi} = \det\left(D\right), \tag{16}$$

where matrix/vector notation has been used in the exponent and the prefactor a^d has been absorbed into D. Z_F is the *fermion partition function* and $\det D$ is usually called the *Dirac* or *fermion determinant*. Additionally, it is possible to integrate out the fermion degrees of freedom of the observable $\mathcal{O}$ to get a new observable

$$\widetilde{\mathcal{O}}[U] = \frac{1}{Z_F} \int \mathcal{D}\big[\overline{\psi}, \psi\big]\, e^{-\overline{\psi} D \psi} \mathcal{O}\left[\overline{\psi}, \psi, U\right], \tag{17}$$

which is dependent only on the gauge links U. With Eq. (16) and Eq. (17) it is now possible to rewrite Eq. (6) to

$$\langle \mathcal{O} \rangle = \frac{1}{Z} \int \mathcal{D}[U]\, e^{-S_G[U]} \det D[U]\; \widetilde{\mathcal{O}}[U]. \tag{18}$$

Here we want to stress that the Dirac operator is of course a functional of the gauge links U. Now, the standard approach of calculating observables in lattice field theory is numerically with Monte Carlo simulations. By applying this idea to Eq. (18), one can consider the Dirac determinant together with the gauge action and the normalization to be a weight factor for generating configurations of the gauge links U distributed with probability $P[U] = \frac{e^{S_G[U]} \det D[U]}{Z}$. Expectation values of observables are then obtained by averaging over these configurations. In order for that to be possible, however, the Dirac determinant has to be real and positive. The reality can easily be verified by using the γ^5-hermiticity of the Dirac operator $\gamma^5 D \gamma^5 = D^\dagger$ via

$$\det\left(D\right)^* = \det(D^\dagger) = \det\left(\gamma^5 D \gamma^5\right) = \det\left(D\right), \tag{19}$$

where γ^5 is defined by $\gamma^5 := i \prod_{\nu=1}^{d} \gamma_\nu$ and by using $(\gamma^5)^2 = \mathbb{1}$ and the anti commutator $\{\gamma_\nu, \gamma^5\} = 0$. To ensure positivity the square of the determinant can be used for example, which amounts to using two different flavors of quarks with the same mass.

This last paragraph shows that the behavior of the Dirac determinant is critical to the numerical calculation of observables. Specifically, if it can no longer be ensured that the determinant is a real quantity, then Monte Carlo simulations are no longer applicable in

a straightforward way. In the next section, where we introduce the chemical potential, we will see that precisely this problem arises.

2.3. Chemical Potential and the Sign Problem

In order to be able to get a detailed understanding of heavy ion collisions and also the inner workings of neutron stars it is necessary to describe QCD at non-zero temperature and non-zero density. The temperature on the lattice can be regulated by compactification of the time direction of the Euclidean lattice by imposing (anti-)periodic boundary conditions for the fields. It can be shown that the temperature is inversely proportional to the lattice extent in time direction. As in statistical mechanics, the inverse temperature is denoted with β[3], which leads to the equation (with k_B set to unity)

$$\beta = aN_d = \frac{1}{T}. \tag{20}$$

To describe non-zero density we need to induce an asymmetry between matter and antimatter. In the lattice description this can be achieved by introducing the additional factors $\exp(\pm a\mu)$ into the hopping matrix from Eq. (15) in the following way

$$H(n|m) = \sum_{\nu=1}^{d} \left\{ [\mathbb{1} - \gamma_\nu]\, U_\nu(n) e^{a\mu\delta_{d\nu}} \delta_{n+\hat{\nu},m} + [\mathbb{1} + \gamma_\nu]\, U_\nu^\dagger(n-\hat{\nu}) e^{-a\mu\delta_{d\nu}} \delta_{n-\hat{\nu},m} \right\}, \tag{21}$$

where μ denotes the chemical potential. To get a conceptual idea of how μ influences the theory, it is necessary to understand the hopping matrix in more detail. Firstly, it is important to note that for each direction ν there are two terms. The first one can be understood as to describe forward hoppings on the lattice, mediated by the gauge links $U_\nu(n)$ and the deltas $\delta_{n+\hat{\nu},m}$. The second term describes backward hoppings, correspondingly. Secondly, it can be seen that due to the delta functions $\delta_{d\nu}$ in the exponent the chemical potential only has an influence in the time direction. This also means, due to the signs in the exponent, that the forward propagation in time is favored, but the backward propagation is suppressed. This introduces the desired asymmetry into the system, since particles can be interpreted as propagating forwards in time, and antiparticles backwards.

The introduction of the chemical potential into the hopping matrix has a drastic effect for the Dirac operator. The additional factors spoil the previously mentioned γ^5-hermiticity, which in turn means that the Dirac determinant is no longer a real quantity. More specifically, it can be shown with the same methods used for Eq. (19) that the

[3] Not to be confused with the inverse gauge coupling, which is also denoted as β.

Dirac operator now obeys

$$\gamma^5 D(\mu)\gamma^5 = D(-\mu)^\dagger. \tag{22}$$

With this, finally, we see the effect of the complex action problem. Since the determinant is now complex it can no longer be interpreted as a probability as in Eq. (18). This makes the standard Monte Carlo approach inapplicable.

There are different approaches available to get a hold of this complex action problem, see for example [5, 6, 7]. One method is to substitute the chemical potential with an imaginary one, $\mu \to i\theta$. The change of sign in the argument of the Dirac operator in Eq. (22) is then corrected by the complex conjugation within the Hermitian conjugation. Therefore, for an imaginary chemical potential the Dirac determinant is real. Of course, when performing this transformation, one has to find a way to relate the physics one wants to study to θ, e.g., by analytical continuation. In this work we will use an imaginary chemical potential in the context of the canonical ensemble that will be discussed in the next chapter.

2.4. Notations

In this short section we want to discuss some notations and fix parameters which were left open in the general discussion so far. First of all, for the rest of this work, we will express all dimensionful quantities in terms of the lattice parameter a. In principle this means that we can set the parameter equal unity, so $a = 1$.

Also, what is especially important for the numerical discussion later on, are the boundary conditions for the fields on the lattice. For the bosonic fields, the gauge links U, we use periodic boundary conditions in all directions. For all fields representing fermionic degrees of freedom, on the other hand, we have periodic boundary conditions in all spatial directions, but anti-periodic boundary conditions in the temporal direction. So this means

$$\begin{aligned} U_\rho(n)|_{n_\nu=0} &= U_\rho(n)|_{n_\nu=N_\nu} && \forall\, \nu,\rho \in \{1,\dots,d\}, \\ \psi(n)|_{n_j=0} &= \psi(n)|_{n_j=N_j} && \forall\, j \in \{1,\dots,d-1\}, \\ \psi(n)|_{n_d=0} &= -\psi(n)|_{n_d=N_d}\,. \end{aligned} \tag{23}$$

For the fields $\overline{\psi}$ apply the same conditions as for ψ.

Another parameter we also need to fix is the number of spacetime dimensions. In this work, we will consider QCD in 1 + 1 dimensions, which means we can set the lattice dimensions to $d = 2$. This also enables us now to give an explicit representation for the

gamma matrices which appear in the hopping matrix. We can set these to

$$\gamma_1 = \sigma_2 = \begin{pmatrix} 0 & -i \\ i & 0 \end{pmatrix}, \qquad \gamma_2 = \sigma_1 = \begin{pmatrix} 0 & 1 \\ 1 & 0 \end{pmatrix},$$

$$\gamma^5 = i\gamma_1\gamma_2 = i\sigma_2\sigma_1 = \sigma_3 = \begin{pmatrix} 1 & 0 \\ 0 & -1 \end{pmatrix},$$

where σ_j are the three Pauli matrices. We also used the previously mentioned definition for the γ^5 matrix. Also, the hopping parameter from Eq. (14) can finally be stated explicitly to be $\kappa = \frac{1}{2m+4}$, with m being the mass of the fermions.

3. Canonical Density of States Method

In this chapter we will discuss a general idea for addressing the sign problem of finite density lattice QCD, namely the density of states method. This ansatz was introduced in [5, 8]. There are different methods of using this approach and we will focus on the specific case where we will work with the canonical ensemble which we introduce as a first step in this chapter. After that, we can state the basic idea and formalism for the canonical density of states method and also give a detailed account on how Monte Carlo simulations can be applied again to calculate observables using the so-called *functional fit approach* [9].

3.1. Canonical Partition Function

As was already discussed in the previous sections, the introduction of the chemical potential gives rise to a sign problem since the Dirac determinant picks up a complex phase. For an imaginary chemical potential, however, no complex factor appears, and to take advantage of this behavior we will change our viewpoint from the previously discussed grand canonical ensemble, where the partition function depends explicitly on the chemical potential $Z(\mu)$, to the canonical ensemble. In this representation, the partition function is no longer a function of μ but depends on the fixed net quark number N_q, which can only assume integer values since it is the total number of quarks minus the number of antiquarks in the system. Positive values can be understood to indicate a surplus of particles, and negative values a surplus of antiparticles. Furthermore, what also needs to be mentioned, is the fact that the absolute value of N_q is bounded due to the finite lattice size. With the spin and color degrees of freedom in mind, it can be seen that each flavor of quarks can contribute a maximum of $6N_1$ (anti-)particles, where N_1 is the number of lattice sites in spatial direction.

To express the canonical partition function, we substitute the chemical potential in the grand canonical partition function as it appears in Eq. (18) with an imaginary one $\mu = i\theta/\beta$ and integrate over θ with an additional Fourier factor $e^{-i\theta N_q}$. This way we can project out the contribution for a specific net number of quarks N_q [2]. This then yields

$$\begin{aligned} Z_{N_q} &= \int_{-\pi}^{\pi} \frac{\mathrm{d}\theta}{2\pi} Z(\mu)\Big|_{\mu=\frac{i\theta}{\beta}} e^{-i\theta N_q} \\ &= \int_{-\pi}^{\pi} \frac{\mathrm{d}\theta}{2\pi} \int \mathcal{D}[U]\, e^{-S_G[U]} \det{}^2 D\,[U,\mu]\Big|_{\mu=\frac{i\theta}{\beta}} e^{-i\theta N_q}, \end{aligned} \tag{24}$$

where β is the inverse temperature as mentioned in Eq. (20) and we squared the determinant to ensure positivity.[4] Alternatively, this formula can also be seen as the inverted

[4] Strictly speaking, this is not a necessary step to take here, as will be discussed in a later chapter where

fugacity expansion of the grand canonical partition function for an imaginary chemical potential. Vacuum expectation values for a fixed quark number can therefore be expressed as

$$\langle \mathcal{O} \rangle_{N_q} = \frac{1}{Z_{N_q}} \int_{-\pi}^{\pi} \frac{\mathrm{d}\theta}{2\pi} \int \mathcal{D}[U]\, e^{-S_G[U]} \det{}^2 D\,[U,\mu]\, \mathcal{O}\,[U,\mu] \Big|_{\mu=\frac{i\theta}{\beta}} e^{-i\theta N_q}, \tag{25}$$

where the observable $\mathcal{O}$ is in general also a function of the chemical potential.

The advantage of this canonical ansatz is that the complex contribution is moved from the determinant to the Fourier moment, which is not dependent on U. This enables us to use Monte Carlo simulations for the gauge link integration. To this end we introduce the density ρ in the next section.

3.2. Density of States

For the canonical partition function we can now define the density of states in the following way

$$\rho^{(\mathcal{J})}(\theta) = \int \mathcal{D}[U]\, e^{-S_G[U]} \det{}^2 D\,[U,\mu]\, \mathcal{J}\,[U,\mu] \Big|_{\mu=\frac{i\theta}{\beta}}. \tag{26}$$

Here, $\mathcal{J}$ is some general real and positive functional of the gauge links and the chemical potential. When we identify this quantity once with some suitable observable $\mathcal{J}[U,\mu] = \mathcal{O}[U,\mu]$ and once with the identity $\mathcal{J}[U,\mu] = \mathbb{1}$, we can express Eq. (25) and Eq. (24) using this density. This yields

$$\begin{aligned} \langle \mathcal{O} \rangle_{N_q} &= \frac{1}{Z_{N_q}} \int_{-\pi}^{\pi} \mathrm{d}\theta \rho^{(\mathcal{O})}(\theta)\, e^{-i\theta N_q}, \\ Z_{N_q} &= \int_{-\pi}^{\pi} \mathrm{d}\theta \rho^{(\mathbb{1})}(\theta)\, e^{-i\theta N_q}, \end{aligned} \tag{27}$$

where we have also cancelled the 2π normalization. This now makes clear why we denoted ρ with the superscript $(\mathcal{J})$, since every observable gives a different density. We also want to stress here that observables which do not satisfy the condition of being real and positive may always be split up into several terms which do fulfill this condition.

The objective in the following will be to find a way to calculate the density $\rho^{(\mathcal{J})}$. This has to be done very precisely due to the integration over θ with the oscillatory Fourier moment. For this we will employ a suitable parametrization of the density. But before we go into detail about that, we want to discuss symmetry properties of the density, which also makes the parametrization simpler.

In general, the density has to be integrated over the symmetric interval $\theta \in [-\pi, \pi]$. But with the help of suitable symmetry transformations, $\rho^{(\mathcal{J})}$ can be classified to be

we will analyze the spectrum of the Dirac operator in detail.

either an even or an odd function, depending on whether $\mathcal{J}$ is even or odd under said transformations.[5] With the use of charge conjugation, for example, it can be shown that $\rho^{(\mathbb{1})}$ is an even function, as it is demonstrated in Appendix A.1 and also in [10, 11]. This property cuts the numerical cost in half, since by using the symmetries the density only needs to be calculated in the reduced interval $\theta \in [0, \pi]$.

Now we can turn to discussing the parametrization for the density. For notational convenience, we will not distinguish the cases with and without insertion of $\mathcal{J}$ but stress that for different insertions the parameters of the density have to evaluated separately. The first step for the parametrization is to divide the reduced interval $[0, \pi]$ into N_θ subintervals

$$[0, \pi] = \bigcup_{n=0}^{N_\theta - 1} I_n, \quad \text{with} \quad I_n = [\theta_n, \theta_{n+1}], \tag{28}$$

where $\theta_0 = 0$ and $\theta_{N_\theta} = \pi$. The length of each interval can then be expressed with $\Delta_n = \theta_{n+1} - \theta_n$.

For the density we use an ansatz that was presented for example in [12],

$$\rho(\theta) = e^{-L(\theta)}, \tag{29}$$

where L is a continuous function which is piecewise linear on the subintervals I_n. Therefore, it can be expressed as

$$L(\theta) = a_n + k_n(\theta - \theta_n), \quad \theta \in I_n. \tag{30}$$

This way we have two parameters per subinterval, the constants a_n as well as the slopes k_n of the lines. What we did not use so far, although, is the fact that we are free to choose a normalization for the densities, since this will cancel out, as can be seen in Eq. (27). If we set $\rho(0) = 1$, this implies $L(0) = 0$[6]. With this normalization, and using also the fact that L is continuous, all the constant factors a_n can be expressed by the slopes k_n and the interval lengths Δ_n. The only unknown parameters for L then are the slopes of all the intervals. With a few lines of algebra it can be shown that L takes the form

$$L(\theta) = d_n + \theta k_n, \quad \theta \in I_n, \quad d_n = \sum_{j=0}^{n-1} (k_j - k_n)\Delta_j. \tag{31}$$

Finally, we can express the density as

$$\rho^{(\mathcal{J})}(\theta) = A_n^{(\mathcal{J})} e^{-\theta k_n^{(\mathcal{J})}}, \quad \theta \in I_n, \quad \text{with} \quad A_n^{(\mathcal{J})} = e^{-d_n^{(\mathcal{J})}}. \tag{32}$$

[5] Here, too, a general $\mathcal{J}$ may always be decomposed into even and odd contributions.

[6] This normalization works fine if the density is even, but would lead to a discontinuity for uneven densities. To avoid this, a different ansatz would be required in that case.

Here we have used the superscript $(\mathcal{J})$ again to make clear that $k_n^{(\mathcal{J})}$ and $A_n^{(\mathcal{J})}$ are in fact dependent on the observable.

What should be noted here, is that the interval size Δ_n can be different for each subinterval I_n. This fact can be used as an advantage for numerical calculations. For example, if the density varies quickly in a given region, the step size can be reduced to get a better approximation. Alternatively, for regions where the density shows slow variations, the step size can be increased to reduce numerical cost. Additionally, larger intervals can also be used to get a rough estimate of the density, to locate the regions of quick variations, for example. Subsequently, the intervals can be refined where necessary. This procedure is called *preconditioning* and will also be mentioned in a later chapter when we discuss our numerical results. For a more detailed account, see for example [9].

With this ansatz, therefore, all that needs to be calculated are the slopes for each of the N_θ subintervals. This can be achieved with a method called the functional fit approach, which is used also for example in [9, 10, 11] and is presented in the next section.

3.3. Functional Fit Approach

The functional fit approach, or FFA for short, is a method to calculate the slopes $k_n^{(\mathcal{J})}$, which will in turn enable us to calculate the density of states as given in Eq. (31) and Eq. (32). For the presentation of this method in this section we will closely follow the steps taken in [10].

First, we define new quantities, the so-called *restricted expectation values* $\langle\theta\rangle_n^{(\mathcal{J})}(\lambda)$ and the corresponding restricted partition functions $Z_n^{(\mathcal{J})}(\lambda)$, which have the following form

$$\begin{aligned}\langle\theta\rangle_n^{(\mathcal{J})}(\lambda) &= \frac{1}{Z_n^{(\mathcal{J})}(\lambda)} \int_{\theta_n}^{\theta_{n+1}} \mathrm{d}\theta \int \mathcal{D}[U]\, e^{-S_G[U]} \det{}^2 D\,[U,\mu]\, \mathcal{J}\,[U,\mu]\,\Big|_{\mu=\frac{i\theta}{\beta}} e^{\lambda\theta}\theta, \\ Z_n^{(\mathcal{J})}(\lambda) &= \int_{\theta_n}^{\theta_{n+1}} \mathrm{d}\theta \int \mathcal{D}[U]\, e^{-S_G[U]} \det{}^2 D\,[U,\mu]\, \mathcal{J}\,[U,\mu]\,\Big|_{\mu=\frac{i\theta}{\beta}} e^{\lambda\theta}.\end{aligned} \tag{33}$$

These expectation values have a very similar form to the actual observables given in Eq. (25) and Eq. (24), but with a few differences. First of all, the integration over the imaginary chemical potential θ is restricted to only one subinterval I_n, which is indicated by the index n. Secondly, the expectation value calculated with this formula is the imaginary chemical potential θ itself. And thirdly, instead of the complex Fourier moment, we have introduced a Boltzmann factor with a real-valued parameter λ which will help us to calculate the slopes. Due to this substitution, the whole integrand is real. Therefore, for this expectation value, no sign problem occurs and Monte Carlo methods are possible, were θ is just an additional degree of freedom in the simulation.

To see how this parameter λ can be used to calculate the slopes $k_n^{(\mathcal{J})}$, we express the

restricted partition function in terms of the density from Eq. (26) by

$$Z_n^{(\mathcal{J})}(\lambda) = \int_{\theta_n}^{\theta_{n+1}} \mathrm{d}\theta \rho^{(\mathcal{J})}(\theta)\, e^{\lambda\theta}. \tag{34}$$

Further, we can use the exponential ansatz from Eq. (32) for the density. In this way we can perform the integration in Eq. (34) analytically to get a closed form expression

$$Z_n^{(\mathcal{J})}(\lambda) = A_n^{(\mathcal{J})} \frac{e^{\theta_n\left(\lambda - k_n^{(\mathcal{J})}\right)}}{\lambda - k_n^{(\mathcal{J})}} \left(e^{\Delta_n\left(\lambda - k_n^{(\mathcal{J})}\right)} - 1 \right). \tag{35}$$

Now, using the fact that the restricted expectation value can be expressed as the derivative of the logarithm of its $Z_n^{(\mathcal{J})}(\lambda)$ with respect to λ, as can easily be verified from Eq. (33), we can use Eq. (35) to obtain

$$\begin{aligned} \langle\theta\rangle_n^{(\mathcal{J})}(\lambda) &= \frac{\mathrm{d}\ln Z_N^{(\mathcal{J})}(\lambda)}{\mathrm{d}\lambda} \\ &= \theta_n + \frac{\Delta_n}{1 - e^{-\Delta_n\left(\lambda - k_n^{(\mathcal{J})}\right)}} - \frac{1}{\lambda - k_n^{(\mathcal{J})}}. \end{aligned} \tag{36}$$

As a last step, we perform an additive and a multiplicative normalization of $\langle\theta\rangle_n^{(\mathcal{J})}(\lambda)$ which yields

$$V_n^{(\mathcal{J})}(\lambda) = \frac{\langle\theta\rangle_n^{(\mathcal{J})}(\lambda) - \theta_n}{\Delta_n} - \frac{1}{2} = h\left(\Delta_n\left[\lambda - k_n^{(\mathcal{J})}\right]\right), \tag{37}$$

where h is a sigmoidal function of the form

$$h(s) = \frac{1}{1 - e^{-s}} - \frac{1}{s} - \frac{1}{2}. \tag{38}$$

At this point we want to state some important properties of this function. These will be useful in a later chapter when we discuss the fitting procedure:

$$\begin{aligned} h(0) = 0, \quad \lim_{s\to\pm\infty} h(s) &= \pm\frac{1}{2}, \\ \left.\frac{\partial h\left(\Delta_n\left[\lambda - k_n^{(\mathcal{J})}\right]\right)}{\partial\lambda}\right|_{\lambda = k_n^{(\mathcal{J})}} &= h'(s)\big|_{s=0}\,\Delta_n = \frac{\Delta_n}{12}. \end{aligned} \tag{39}$$

Here we want to emphasize the equation given in the second line, which states that the slope of the function at its root is dependent on the size of the interval Δ_n. This is an helpful fact which can be used later on as a check for consistency of our calculations.

With this result we are now able to approximate the slopes $k_n^{(\mathcal{J})}$ which we need to evaluate the density. As the first step of this procedure, $\langle\theta\rangle_n^{(\mathcal{J})}(\lambda)$ from Eq. (33) can be

calculated numerically with Monte Carlo methods. This needs to be done for several values of the real parameter λ. Since we can choose its values freely, this can be used as an advantage. For a negative value of λ, for example, the integral is exponentially suppressed for higher values of θ. Therefore, the lower part of the integration is the dominant factor in the result. Conversely, for a positive λ, the upper part of the integral contributes stronger. This shows that this parameter can be used to scan the subintervals I_n even more precisely.

Following the Monte Carlo simulations we can perform the normalizations given in Eq. (37) to get $V_n^{(\mathcal{J})}(\lambda)$. This numerical data can then be used to fit the function h, where the only parameter in this function which is not known is $k_n^{(\mathcal{J})}$. Therefore, a one parameter fit can be used to get an estimate for the slope. This procedure has to be repeated for all subintervals I_n and the results can then be used to calculate the density $\rho^{(\mathcal{J})}(\theta)$ with Eq. (32). All this needs to be done twice, once for some observable $\mathcal{J}[U,\mu] = \mathcal{O}[U,\mu]$ and once for $\mathcal{J}[U,\mu] = \mathbb{1}$. Finally, the vacuum expectation value for a fixed net quark number N_q can be obtained after the integrations in Eq. (27).

This concludes our discussion of the technical description of the canonical density of states approach. What still needs to be addressed is how the Dirac determinant in Eq. (33) will be calculated, since this is a very costly task in terms of computer time. We aim to employ Monte Carlo simulations for this quantity too. The ansatz how this can be achieved is discussed in the next chapter.

4. Multi-Boson Representation of the Dirac Determinant

In this chapter we will discuss a method for calculating the Dirac determinant using auxiliary bosonic fields. This is obviously a central quantity in our simulation, since it appears in the restricted expectation value in Eq. (33) which we aim to calculate with Monte Carlo methods. Therefore we are in need of an efficient method to evaluate this determinant.

4.1. Pseudofermions

Before we discuss some of the possible approaches to calculating the determinant, we will at first take a step back to remind ourselves where the expression for the determinant originates. From Eq. (16) we see that it can be written as an Gaussian integral over the fermion degrees of freedom. The problem with this expression is, however, that the fields $\overline{\psi}$ and ψ are Grassmann-valued. The numerical implementation of these variables is very challenging and does not give rise to efficient algorithms. Also, standard algorithms for calculating determinants are numerically rather expensive, especially for larger matrices. Therefore we are looking for a different way to represent this determinant.

To achieve that, we introduce, in analogy to the fermionic Gaussian integral, a bosonic Gaussian integral. This means that instead of Grassmann variables we now work with a complex field ϕ. For this type of integral holds a similar identity to that of Eq. (16), namely [3]

$$\int \mathcal{D}[\phi]\, e^{-\phi^\dagger M \phi} = \frac{\pi^n}{\det M}. \tag{40}$$

Here, the integral measure is defined as $\int \mathcal{D}[\phi] = \prod_{k=1}^{n} \int_{\mathbb{C}} \mathrm{d}\phi_k$ and n is the dimension of the matrix M. For this expression to be correct, a sufficient condition is that the matrix M is hermitian, $M = M^\dagger$, and the spectrum of M is positive definite. Additionally, since with these conditions M is invertible, the equation $\frac{1}{\det M} = \det M^{-1}$ holds. We then can write the determinant as

$$\det M = \pi^{-n} \int \mathcal{D}[\phi]\, e^{-\phi^\dagger M^{-1} \phi}. \tag{41}$$

Now if we turn back to Eq. (33), we see that in fact we want to calculate the square of the Dirac determinant. This can be rewritten to

$$\det D \det D = \det D^\dagger \det D = \det(D^\dagger D),$$

where in the first step we have used the γ^5-hermiticity of the Dirac operator, which holds for imaginary chemical potential. If we now identify $M = D^\dagger D$ in Eq. (41), we see that we have an expression for the fermion determinant using a path integral over bosonic

degrees of freedom, as was introduced in [13]. The field ϕ is therefore often referred to as *pseudofermions*.

Still, this is not an ideal representation of the determinant for numerical implementation. The problem here lies in the fact that the inverse of the matrix has to be calculated. This is numerically very expensive, since the size of the matrix scales with the lattice size, and also with the number of spacetime dimensions. Additionally, since the determinant is part of the weight in the Monte Carlo simulation, it has to be calculated for every configuration of the gauge links U. This means that a direct implementation of Eq. (41) is accompanied with a too high numerical effort. Therefore, in the next section, we discuss a factorization of the determinant which helps us to find an approximate solution that can also be combined with the pseudofermion method.

4.2. Chebyshev Factorization of the Dirac Determinant

In this section we introduce a convenient factorization which we will use to express the Dirac determinant. This, in turn, will enable us to adopt the above mentioned pseudofermion representation to approximate the determinant in a numerically less expensive way. At the heart of this factorization lie the Chebyshev polynomials, therefore we will call this the *Chebyshev factorization*. This method is explained for example in [14, 15].

As a first step, we will discuss this factorization for a single complex number z. This number has to be contained within an ellipse which does not touch the origin and whose center, denoted by d, lies on the positive real axis. If we define the semi-major and semi-minor axes to be called a and b respectively, we can express the linear eccentricity of this ellipse as $c = \sqrt{a^2 - b^2}$. In this case it is possible to approximate the inverse of z with a polynomial P_N

$$\frac{1}{z} \approx P_N(z) = c_N \prod_{j=1}^{N} (z - z_j), \tag{42}$$

where N is the degree of the polynomial and c_N is a normalization constant which depends on N. The z_j are the roots of P_N which can be explicitly calculated by using properties of the Chebyshev polynomials. They lie on a larger ellipse which passes through the origin and encloses the other ellipse. They are given by

$$z_j = d\left(1 - \cos\left(\frac{2\pi j}{N+1}\right)\right) - i\sqrt{d^2 - c^2}\,\sin\left(\frac{2\pi j}{N+1}\right), \tag{43}$$

with $j = 1, \ldots, N$. The center of this ellipse is also given by d and it also shares the same linear eccentricity c. The factorization of Eq. (42) is therefore in principle possible for all z with $\mathrm{Re}(z) > 0$. Also, we are going to assume that N is an even number, because then the z_j always come in complex conjugate pairs, as can be checked with Eq. (43).

This will be convenient later on.

For our purposes, however, we need to generalize this ansatz from complex numbers to matrices. To this end, consider a diagonalizable matrix[7] $M = S^{-1}JS$ with a nonsingular matrix S and $J = \mathrm{diag}(\lambda_1, \ldots, \lambda_n)$, where λ_k, $k = 1, \ldots, n$ are the eigenvalues of M and n is its dimension. This means that a polynomial of the matrix can be written as

$$P_N(M) = P_N(S^{-1}JS) = S^{-1}P_N(J)S = S^{-1}\mathrm{diag}(P_N(\lambda_1), \ldots, P_N(\lambda_n))S. \tag{44}$$

Here, the last step is possible since J is a diagonal matrix, which means that none of the entries mix in the polynomial. Now we can use the equality in Eq. (42) for each entry of the matrix separately and then pull the product out of the diagonal matrix to write

$$P_N(M) = S^{-1}\left[c_N \prod_{j=1}^{N}(J - z_j\mathbb{1})\right] S = c_N \prod_{j=1}^{N}(M - z_j\mathbb{1}). \tag{45}$$

Additionally, if we use the approximation in Eq. (42), then Eq. (44) yields

$$P_N(M) \approx S^{-1}\mathrm{diag}\left(\frac{1}{\lambda_1}, \ldots, \frac{1}{\lambda_n}\right) S = S^{-1}J^{-1}S = M^{-1}. \tag{46}$$

When comparing Eq. (45) and Eq. (46), one can see that the inverse of a diagonalizable matrix M can be expressed by a polynomial similar to the one for a single complex number as in Eq. (42), required that all the eigenvalues of the matrix obey $\mathrm{Re}(\lambda_k) > 0$ so that the spectrum of M can be enclosed by an ellipse described by Eq. (43).

We can now use Eq. (45) and Eq. (46) to express the determinant of M with the Chebyshev factorization. To this end, we can use the relation $\frac{1}{\det M} = \det M^{-1}$ which holds for invertible matrices. After rearranging the equation, this yields

$$\det M \approx \widetilde{c}_N \prod_{j=1}^{N} \frac{1}{\det(M - z_j\mathbb{1})}, \tag{47}$$

where $\widetilde{c}_N = \frac{1}{c_N}$.

Now, having found an expression to calculate the determinant of some general diagonalizable matrix M with a spectrum in the positive real half-plane, we would like to turn back to look at our matrix of interest, the Dirac operator. But before we can employ the Chebyshev factorization in this case, we need to check if the eigenvalues fulfill the requirement that they can be enclosed by the ellipse as discussed above. This problem will be dealt with in the next section where we will take a closer look at the spectrum of

[7] In fact, this factorization also works for non-diagonalizable matrices [15]. But in this thesis we only need to concern ourselves with diagonalizable ones.

the Dirac determinant in the free case, where the gauge links are set to unity, and also discuss it for the full theory, where the gauge links are included. There we will find that this factorization is indeed viable for the Dirac determinant. But for the moment, to finish the discussion, we assume that all the requirements for the spectrum are fulfilled and insert Eq. (14) in Eq. (47), which yields

$$\det D = \det(\mathbb{1} - \kappa H) \approx \widetilde{c}_N \prod_{j=1}^{N} \frac{1}{\det((1-z_j)\mathbb{1} - \kappa H)} = \widetilde{c}_N \prod_{j=1}^{N} \frac{1}{\det(u_j \mathbb{1} - \kappa H)}, \quad (48)$$

where we have defined $u_j = 1 - z_j$.

As can be seen now from Eq. (48), we are able to approximate the Dirac determinant as a product of N inverse determinants. Our aim is now to express these inverse determinants using bosonic Gaussian integrals as in Eq. (40). In order to establish that this is possible we now show that the matrices are hermitian and then also demonstrate that the eigenvalues are positive. We can use the second Dirac determinant to fulfill this condition. If we introduce the shorthand $D_j = u_j \mathbb{1} - \kappa H$ we can write

$$\begin{aligned}
\det{}^2 D &= \det D^\dagger \det D \\
&\approx \widetilde{c}_N^2 \prod_{j=1}^{N} \frac{1}{\det(u_j \mathbb{1} - \kappa H^\dagger)} \frac{1}{\det(u_j \mathbb{1} - \kappa H)} \\
&= \widetilde{c}_N^2 \prod_{j=1}^{N} \frac{1}{\det(D_j^\dagger D_j)} \\
&= s_N \prod_{j=1}^{N} \int \mathcal{D}\left[\phi^{(j)}\right] e^{-\phi^{(j)\dagger} D_j^\dagger D_j \phi^{(j)}}. \qquad (49)
\end{aligned}$$

In the first step we used the γ^5-hermiticity of the Dirac operator and then we employed the approximation from Eq. (48). For the third line we used the fact that the u_j always appear in complex conjugate pairs. In the last step we could make use of Eq. (40), since $D_j^\dagger D_j$ is obviously a hermitian matrix, and thereby introduced N bosonic fields $\phi^{(j)}$, $j = 1, \ldots, N$. These fields of course also carry Dirac and color indices, but these are suppressed for notational convenience. s_N is a constant factor which combines $\widetilde{c}_N^2$ with the constants from Eq. (40). We will not concern ourselves here with the explicit form of this constant, since it appears in the numerator as well as in the denominator of the restricted expectation value in Eq. (33) and therefore cancels out.

As a final step, we want to absorb the product which appears in Eq. (49) into the definition of the path integral measure via $\prod_{j=1}^{N} \int \mathcal{D}\left[\phi^{(j)}\right] = \int \mathcal{D}[\phi]$. The product of exponentials can then be written as a sum in the exponent. This means that we can

approximate the squared Dirac determinant as

$$\det{}^2 D \approx \int \mathcal{D}[\phi]\, e^{-\sum_{j=1}^{N} \phi^{(j)\dagger} D_j^\dagger D_j \phi^{(j)}}, \tag{50}$$

where we now have also dropped the normalization s_N.

As a summary of this chapter so far, we want to discuss what this Chebyshev factorization entails for our calculation. As can be seen when comparing Eq. (41) with Eq. (50), we were able to circumvent the necessity of inverting matrices, which is a very time consuming task for large matrices. But in exchange, we now do not only have one bosonic field in the path integral, but N species. Due to this fact this ansatz is often called *multi-boson representation* of the Dirac determinant. As a next step it is of course necessary to investigate how many of the fields $\phi^{(j)}$ are needed to achieve a good approximation for the determinants. This will be studied in the next chapter. At first, however, we take a look at the spectrum of the Dirac operator to show that the Chebyshev approximation is applicable at all.

4.3. Eigenvalues of the Dirac Operator

In this section we are going to verify that the spectrum of the Dirac operator has the properties that are required for the Chebyshev factorization. To this end, we separate the discussion into two parts. First, we will talk about the spectrum of a simplified version of the theory where we are working with the so-called *free Dirac operator*. In this case it is possible to calculate the spectrum analytically. The second part of the discussion, where we will talk about the full theory, will be kept very short. There we will give only a short account on why the factorization works and will refer to the literature for a detailed description. With the results of this analysis we are then able to determine the open parameters of the ellipse in Eq. (43).

4.3.1. Free Dirac Operator

The simplified version using the free Dirac operator describes a system where the quarks on different lattice sites do not interact with one another. Since the interaction is governed by the gauge links U, the free theory can be described by setting all gauge links equal to unity, $U_\nu(n) = \mathbb{1}, \forall\, \nu, n$. The free Dirac operator can thus still be written as in Eq. (14), but the hopping matrix from Eq. (21) now simplifies to

$$H(n|m) = \sum_{\nu=1}^{2} \left\{ [\mathbb{1} - \gamma_\nu]\, e^{\frac{i\theta}{\beta}\delta_{\nu,2}} \delta_{n+\hat{\nu},m} + [\mathbb{1} + \gamma_\nu]\, e^{-\frac{i\theta}{\beta}\delta_{\nu,2}} \delta_{n-\hat{\nu},m} \right\}, \tag{51}$$

where we now already inserted the imaginary chemical potential via $\mu = \frac{i\theta}{\beta}$.

When calculating the spectrum of the free Dirac operator it is convenient to first perform a Fourier transformation to momentum space, because then the matrix becomes block diagonal, as is demonstrated in Appendix A.2. This reduces the complexity of the problem greatly, since the spectrum of a block diagonal matrix is given by the combined spectrum of all the individual blocks. This means we now only need to calculate the eigenvalues of the two by two matrices $\widetilde{D}'(p)$ from Eq. (A.4) for all values of the discretized momenta $p^T = (p_1, p_2)$ given in Eq. (A.2). By setting $\det\left(\widetilde{D}'(p) - \lambda \mathbb{1}\right) \stackrel{!}{=} 0$, we can calculate the eigenvalues of the free Dirac operator to be

$$\lambda_{\pm}(p) = 1 - 2\kappa\left(\cos(p_1) + \cos(p_2')\right) \pm i2\kappa\sqrt{\sin^2(p_1) + \sin^2(p_2')}, \tag{52}$$

where we used the abbreviation p_2' defined in Eq. (A.5).

With this result for the eigenvalues, we can now check the region to which the spectrum of the Dirac operator is confined to in the free case of the theory. Using the lower and upper bounds of the trigonometric functions it is easy to verify that all the eigenvalues lie within

$$\begin{aligned} 1 - 4\kappa \leq \mathrm{Re}\left(\lambda_{\pm}(p)\right) \leq 1 + 4\kappa, \\ -\sqrt{8}\kappa \leq \mathrm{Im}\left(\lambda_{\pm}(p)\right) \leq \sqrt{8}\kappa. \end{aligned} \tag{53}$$

For the real part of the spectrum we can now see that the crucial requirements for the Chebyshev factorization can be fulfilled if the hopping parameter κ is chosen to be $\kappa < \frac{1}{4}$, which implies for the mass of the fermions that it has to be larger than zero. In that case the real part of the eigenvalues does not touch the origin since it is confined to $\mathrm{Re}(\lambda_{\pm}(p)) \in (0, 2)$, which means it is possible to define an ellipse according to Eq. (43) which encloses the whole spectrum of the free Dirac operator.

What is also important to note is that the spectrum does in fact not only depend on the mass m via the hopping parameter κ, but also on the imaginary chemical potential θ through p_2'. In order to get a more detailed understanding of how these parameters influence the eigenvalues, we have plotted the spectrum of the free Dirac operator for several combinations of these parameters in Fig. 1 for an 8×8 lattice.

As can be seen in Fig. 1a, where the imaginary chemical potential was fixed to $\theta = \pi/2$, increasing the mass leads just to an overall contraction of the spectrum. The variation of θ in Fig. 1b, however, does not change the extent of the spectrum in any way but only shifts the eigenvalues within the general shape of the spectrum. Additionally, as can of course be seen in Eq. (52), the eigenvalues always come in complex conjugate pairs. What we also want to mention is that for larger lattices the extent of the spectrum does of course also not change. The only effect this has is that the general shape that can be seen in Fig. 1 becomes more densely populated with eigenvalues.

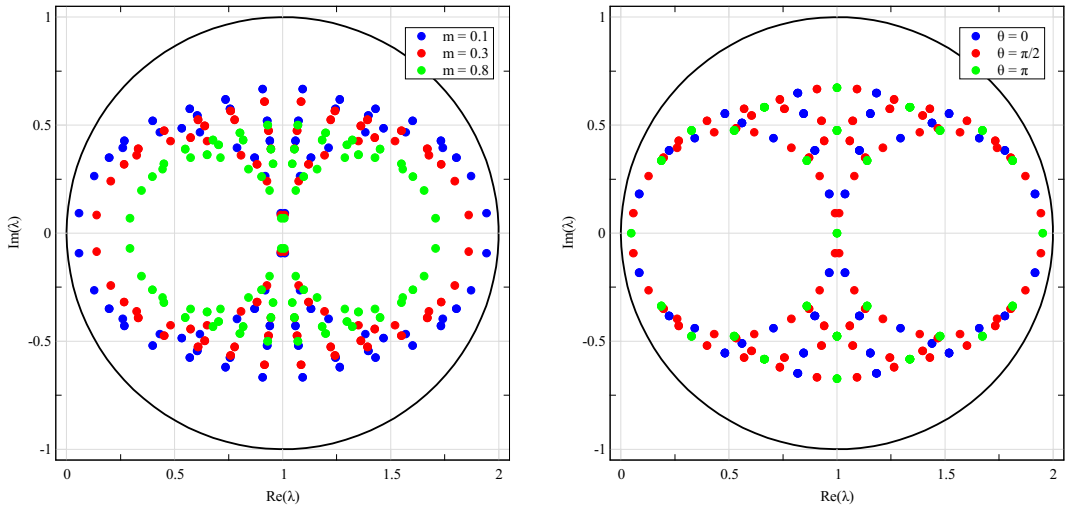

(a) $\theta = \pi/2$. (b) $m = 0.1$.

Fig. 1: The spectrum of the free Dirac operator on an 8×8 lattice for different values of (a) the mass m and (b) the imaginary chemical potential θ. Also the ellipse (black circle) for the Chebyshev factorization is plotted.

4.3.2. Complete Dirac Operator

In this section we are looking at the behavior of the complete Dirac operator, which includes the gauge links U. Here it is also possible to show that all the necessary conditions needed for the Chebyshev factorization are fulfilled by the spectrum. We will, however, not give a detailed presentation of how this can be seen, but refer to the literature instead. In [10], for example, a crude estimate for the lower bound of the spectrum is given for a real chemical potential. For an imaginary chemical potential it is then easy to see that the same estimation yields that the spectrum of the Dirac operator does not touch the origin for $m > 0$, the same result as for the free Dirac operator. Additionally, as it is also mentioned in [10], the introduction of gauge links into the free Dirac operator leads only to a contraction of the spectrum. That means that an ellipse which encloses the free spectrum does also enclose the eigenvalues of the full Dirac operator.

What we also want to discuss at this point is the fact that we squared the Dirac determinant in order to ensure positivity, as we mentioned earlier when we introduced the canonical partition function. This is in fact not necessary, as can be shown when looking at the eigenvalues of the Dirac operator. Using the γ^5-hermiticity from Eq. (22) for an imaginary chemical potential, which uses just a unitary transformation, it is easy to see that the spectrum of D is the same as the spectrum of $D^\dagger$. This shows that the eigenvalues always appear in complex conjugate pairs, discussed for example also in [16]. Since also $\mathrm{Re}(\lambda_\pm(p)) > 0$ holds, we know that the Dirac determinant is real and positive

by itself. Moreover, this also ensures that the spectrum of $D_j^\dagger D_j$ is positive definite, which we mentioned is a sufficient condition for the last step in Eq. (49). Additionally, we also do not need the second Dirac determinant to ensure hermiticity in Eq. (49), as will be used in a following chapter.

All this shows that for the canonical density of states method it is not required to work with an even number of mass degenerate quarks. In this thesis, however, we will continue to work with two mass degenerate flavors, since this is already a good approximation for the behavior of the two lightest quarks, up and down, which have similar masses [1]. But if the inclusion of additional quarks or quarks with different masses is desired, it can be accomplished in a straightforward way.

Turning back to the spectrum of the Dirac operator, we can now use our knowledge of the behavior of the eigenvalues to fix the open parameters of the ellipse in the Chebyshev factorization. A straightforward way to do this is to set d to the center of the spectrum, $d = 1$, and to set the linear eccentricity to $c = 0$. This defines a circle, which is also plotted in Fig. 1. The quantities u_j that appeared in the Chebyshev factorization of the Dirac determinant in Eq. (48) can then be expressed in the simple form of a unit circle,

$$u_j = 1 - z_j = e^{i\frac{2\pi j}{N+1}}. \tag{54}$$

With this we can now conclude this chapter. We were able to show that the spectrum of the Dirac operator fulfills all the properties required for the Chebyshev factorization also for non-zero imaginary chemical potential, see Eq. (53) and Fig. 1. Therefore, we can approximate the squared Dirac determinant with complex Gaussian integrals using several pseudofermion fields $\phi^{(j)}$ via Eq. (50). In the next chapter we will use this ansatz and the free Dirac determinant for first numerical calculations, where we will be able to verify the results with exact analytic solutions. This will tell us how many Chebyshev factors N are needed to obtain a good approximation of the determinant.

5. Testing the Chebyshev Factorization

In this chapter our goal is to perform first tests using the Chebyshev factorization of the free Dirac determinant. Following that, we will also perform a first Monte Carlo simulation using the pseudofermion ansatz. We will work with the free Dirac operator because this simplified theory has the advantage that observables can be computed analytically. This enables us to verify the calculations using the factorization of the determinant with the exact results. The quantities of interest in this chapter are the *free energy* and the *chiral condensate*, which will be introduced in detail in the first section. After that, we will calculate these quantities for different numbers of Chebyshev factors N, as well as for different values of the other free parameters of our theory, for example the mass of the fermions. This will help us to identify a suitable amount of Chebyshev factors N which give a good approximation of the Dirac determinant. This result will be important afterwards when we implement the pseudofermion ansatz of the determinant using Monte Carlo methods.

Since in this chapter our main focus is the Chebyshev factorization, we will not perform any θ integrations. This means the calculated quantities will always depend on the imaginary chemical potential, which is therefore also a free parameter in this discussion. Also, for these tests, it is sufficient if we work with one quark flavor.

5.1. Free Energy and Chiral Condensate

The quantities for which we are going to test the factorization are the free energy and the chiral condensate, denoted as F and $\langle\overline{\psi}\psi\rangle$ respectively. Since we are working with the canonical ensemble, the free energy represents the corresponding thermodynamic potential and is given by $F = -\frac{1}{\beta}\ln\left(Z_{N_q}\right)$, which is explained in any textbook on statistical physics. We will not work with the full form of the canonical partition function from Eq. (24), however, but with a simplified version. As already mentioned, we are not performing the θ integration, so we leave it out together with the Fourier factor. Also, since we are working with the free theory without interactions between the fermions, we set $U_\nu(n) = \mathbb{1}, \forall\, \nu, n$. By doing so the gauge action and the path integral over the gauge links drop out, as can be seen in Eq. (10) and by the fact that the Haar measures are already suitably normalized [2]. Since we are only working with one flavor, the partition function is now reduced to

$$\widetilde{Z}(\theta) = \det D(\mu)\big|_{\mu=\frac{i\theta}{\beta}}. \tag{55}$$

This is equivalent to the free grand canonical partition function with an imaginary chemical potential. Using this $\widetilde{Z}$, the free energy reduces to

$$F = -\frac{1}{\beta}\ln\left(\det D\right), \tag{56}$$

where the dependence on the imaginary chemical potential is suppressed in our notation.

The second quantity, an observable called the chiral condensate $\langle\overline{\psi}\psi\rangle$, is important in phenomenological descriptions of QCD and is used as an order parameter for phase transitions due to the spontaneous[8] breaking of chiral symmetry in the limit of massless fermions, called the *chiral limit*. Although this is an interesting topic, we will not go into further detail about the physics of the chiral condensate, since our focus is now just on the numerical implementation of the Chebyshev expansion. For more information about the chiral condensate on the lattice and the continuum the reader is referred to [2, 17] and [18].

For our definition of $\langle\overline{\psi}\psi\rangle$ the same simplifications as above will be used for Eq. (25). In this equation the fermion degrees of freedom are already integrated out, and therefore the observable cannot depend on the fermion fields. To express the chiral condensate we need to reverse that step by writing the Dirac determinant as a fermionic Gaussian integral as in Eq. (16) where we can then set the observable to $\mathcal{O} = \overline{\psi}\psi$. Then we can write the chiral condensate as (cf. Eq. (17))

$$\begin{aligned}\langle\overline{\psi}\psi\rangle &= \frac{1}{V\widetilde{Z}}\int\mathcal{D}\big[\,\overline{\psi},\psi\big]\, e^{-\overline{\psi}D\psi}\overline{\psi}\psi \\ &= \frac{-1}{V}\frac{\partial}{\partial s}\ln\left(\det D_s\right)\Big|_{s=1}. \end{aligned} \tag{57}$$

Here we used the lattice volume $V = N_1N_2$ as an additional normalization and also introduced the parameter s in the Dirac operator via $D_s = s\mathbb{1} - \kappa H$, which is set to one after taking the derivative. This way we can express $\langle\overline{\psi}\psi\rangle$ by using the Dirac determinant. The validity of the second line can be easily verified when remembering Eq. (16). Also, we again use the hopping matrix H, which for both the free energy and the chiral condensate is given by Eq. (51).

The reason why we chose these two quantities for our tests is because they have a very simple dependence on the Dirac determinant, as can be seen from Eq. (56) and Eq. (57). This enables us to test the Chebyshev factorization efficiently. In the case of the chiral condensate it is further possible to express the determinant with pseudofermions and calculate $\langle\overline{\psi}\psi\rangle$ using Monte Carlo simulations, as will be explained later in this section. But at first we will show how the logarithm of the determinant can be expressed by using the Fourier transform of the Dirac operator, which is calculated in Appendix A.2. Since $\widetilde{D}\,(p|q)$ in Eq. (A.3) is block diagonal, its determinant reduces to the product of the determinants of the blocks $\widetilde{D}'(p)$ in Eq. (A.4). Additionally, when writing the logarithm

[8] In our lattice description, using the Wilson-Dirac operator, the chiral symmetry is always broken explicitly. However, this problem can be cured if instead of the Wilson term a so-called *Ginsparg-Wilson* Dirac operator is used [2, 17].

of products as a sum of logarithms we have

$$\begin{aligned}\ln\left(\det D_s\right) &= \ln\left(\det\left[s\mathbb{1}-\kappa H\right]\right)\\ &= \ln\left(\prod_p \det \widetilde{D}'_s(p)\right)\\ &= \sum_p \ln\left(\left[s-2\kappa(\cos(p_1)+\cos(p'_2))\right]^2+4\kappa^2\left[\sin^2(p_1)+\sin^2(p'_2)\right]\right), \qquad (58)\end{aligned}$$

where the propagation of s through the calculation of the Fourier transformation is straightforward.

Now we will use the Chebyshev factorization to express the quantity $\ln\left(\det D_s\right)$. As a first step, we use Eq. (48) for the determinant of D_s. Here we have to be careful, however, since we introduced the parameter s and this formula works only for matrices of the form $\mathbb{1}-M$. With that in mind we can write

$$\begin{aligned}\det D_s &= \det\left(s\mathbb{1}-\kappa H\right)\\ &\approx \widetilde{c}_N s^{2V}\prod_{j=1}^{N}\frac{1}{\det\left(u_j-\frac{\kappa}{s}H\right)}\\ &= \widetilde{c}_N s^{2V(1+N)}\prod_{j=1}^{N/2}\frac{1}{|\det\left(su_j\mathbb{1}-\kappa H\right)|^2}. \qquad (59)\end{aligned}$$

For the second line we first pulled the factor s out of the determinant to obtain the desired form of the matrix, where the exponent of s is the dimension of the Dirac operator. The factor 2 comes from the gamma matrices in two dimensions, and V is the size in real space, given by the volume of the lattice. The gauge links do not contribute since they are set to unity. Following that, also for the second line, we used the Chebyshev factorization. This is possible since we know that the parameter s is in the vicinity of 1, otherwise we would need to check if the spectrum of the matrix in the determinant is still compatible with the restrictions of the ellipse. For the third line we now pulled the factor $\frac{1}{s}$ out of the determinant and then used the γ^5-hermiticity of H together with the fact that the u_j always come in complex conjugate pairs, which is the case since we chose N to be even.

At this point it is also necessary to calculate the normalization $\widetilde{c}_N$ explicitly, since it does not drop out in the calculation of the free energy. This can be easily done with Eq. (47) and the requirement that $\det\mathbb{1}=1$. Using also that the u_j come in complex conjugate pairs and lie on the unit circle, see Eq. (54), this yields the particularly simple answer

$$\widetilde{c}_N = 1. \qquad (60)$$

Putting Eq. (59) and Eq. (60) together, we can write the logarithm of the Dirac

determinant using the Chebyshev factorization as

$$\ln\left(\det D_s\right) \approx 2V(1+N)\ln(s) - \sum_{j=1}^{N/2} \ln\left(\left|\det\left(su_j\mathbb{1} - \kappa H\right)\right|^2\right). \tag{61}$$

For the remaining determinant in the logarithm we can use the same analytical expression as was used in Eq. (58), only that the scalar s is now also accompanied by the complex numbers u_j. So for both expressions Eq. (58) and Eq. (61) we use the analytic results, but for the latter we also employed the Chebyshev factorization which gives us a simple way to test the quality of this approximation.

With these results for $\ln\left(\det D_s\right)$ it is now easy to calculate the analytic result of the free energy F_{an} by using Eq. (58) with $s = 1$ and by using the prefactors of Eq. (56). And in the same way, via Eq. (61), we can approximate the free energy with the Chebyshev factorization, which we call F_{Ch}. In the same spirit we can also calculate the analytic and the approximated chiral condensate $\langle\overline{\psi}\psi\rangle_{an}$ and $\langle\overline{\psi}\psi\rangle_{Ch}$, respectively, where taking the derivative in Eq. (57) is a straightforward calculation. In the next section we compare the numerical results for all these quantities.

Before we do that, however, we also want to discuss how the chiral condensate can be used to test the implementation of the multi-boson representation of the free Dirac determinant. This can be done via Monte Carlo simulations and is a stand-alone calculation, needing no analytical input, and could in principle also be extended to the full theory including the gauge links. We will, however, stay with the free theory where we have analytical data to which we can compare our results to.

The first step now is to express the Dirac determinant using the pseudofermion fields $\phi^{(j)}$ to find an expression for the chiral condensate which can be evaluated with Monte Carlo methods. This can be achieved by using the Chebyshev approximation as in Eq. (59), where we can use the fact that the absolute square of any determinant can be written as $|\det M|^2 = \det\left(M^\dagger M\right)$. This shows that it is also possible to use Eq. (49) and therefore Eq. (50) for only a single determinant, i.e. only one flavor, where the difference is that in this way the number of pseudofermion fields reduces to $N/2$. This can be understood by the fact that removing one determinant corresponds to removing one quark flavor, which cuts the fermion degrees of freedom in the theory in half.

Putting these equations together we can immediately express the logarithm of the free Dirac determinant as

$$\ln\left(\det D_s\right) \approx 2V(1+N)\ln(s) + \ln\left(\int \mathcal{D}[\phi]\, e^{-\sum_{j=1}^{N/2} {\phi^{(j)}}^\dagger [su_j\mathbb{1}-\kappa H]^\dagger [su_j\mathbb{1}-\kappa H]\phi^{(j)}}\right). \tag{62}$$

Here we already ignored the normalization s_N from Eq. (49) since it drops out when we insert this result in Eq. (57). The derivative with respect to the parameter s can be

calculated within a few lines of algebra. The chiral condensate, expressed with pseudo-fermions, can then be written in the compact form

$$\langle\overline{\psi}\psi\rangle \approx -2(1+N) + \frac{1}{V}\left\langle \sum_{j=1}^{N/2} \phi^{(j)\dagger}\left[2\mathbb{1} - \kappa\left(u_j^* H + u_j H^\dagger\right)\right]\phi^{(j)} \right\rangle . \tag{63}$$

Here, the expression within the angle brackets denotes the observable we will calculate with Monte Carlo simulations. Using some general observable $\mathcal{O}$, these brackets can be expressed as the path integral over the fields $\phi^{(j)}$ by

$$\begin{aligned} \langle\mathcal{O}\rangle &= \frac{1}{Z}\int \mathcal{D}[\phi]\, e^{-\sum_{j=1}^{N/2}\phi^{(j)\dagger} D_j^\dagger D_j \phi^{(j)}}\mathcal{O}\,[\phi]\,, \\ Z &= \int \mathcal{D}[\phi]\, e^{-\sum_{j=1}^{N/2}\phi^{(j)\dagger} D_j^\dagger D_j \phi^{(j)}}. \end{aligned} \tag{64}$$

The implementation of Eq. (63) and the numerical results will only be discussed after the next section, since before that, as already mentioned, we compare the results for F_{an} and F_{Ch} as well as for $\langle\overline{\psi}\psi\rangle_{an}$ and $\langle\overline{\psi}\psi\rangle_{Ch}$.

5.2. Numerical Results for the Chebyshev Factorization

In this section we present and discuss our first numerical results using the Chebyshev factorization of the free Dirac determinant. To this end, we look at the relative error between the analytic and the approximated results

$$\varepsilon = \frac{|X_{an} - X_{Ch}|}{X_{an}},$$

where X is to be substituted with F or $\langle\overline{\psi}\psi\rangle$ to obtain the relative error for the free energy or the chiral condensate, respectively. This is done for several combinations of the mass m, the imaginary chemical potential θ, the lattice size $N_1 \times N_2$ as well as the number of Chebyshev factors N, to see how these parameters influence the quality of the approximation. The results of these calculations can be seen in Fig. 2.

Starting our discussion with the first plot, Fig. 2a, where the results for an 128×128 lattice and an imaginary chemical potential of $\theta = 0$ is shown, we can see that the convergence of the Chebyshev approximation is roughly of exponential form in the displayed region of N. What can also be seen is the fact that the approximation is better for fermions with larger masses m. The reason for that is the *spectral gap* (see, e.g., [14]), which defines the minimal distance between the eigenvalues of the Dirac operator and the circle defined by the z_j from Eq. (43). It can be shown that the convergence is better for larger spectral gaps. Since this gap is given by $1 - 4\kappa$, the lower bound of the real part of the eigenvalues from Eq. (53), it is clear that the gap increases for larger masses,

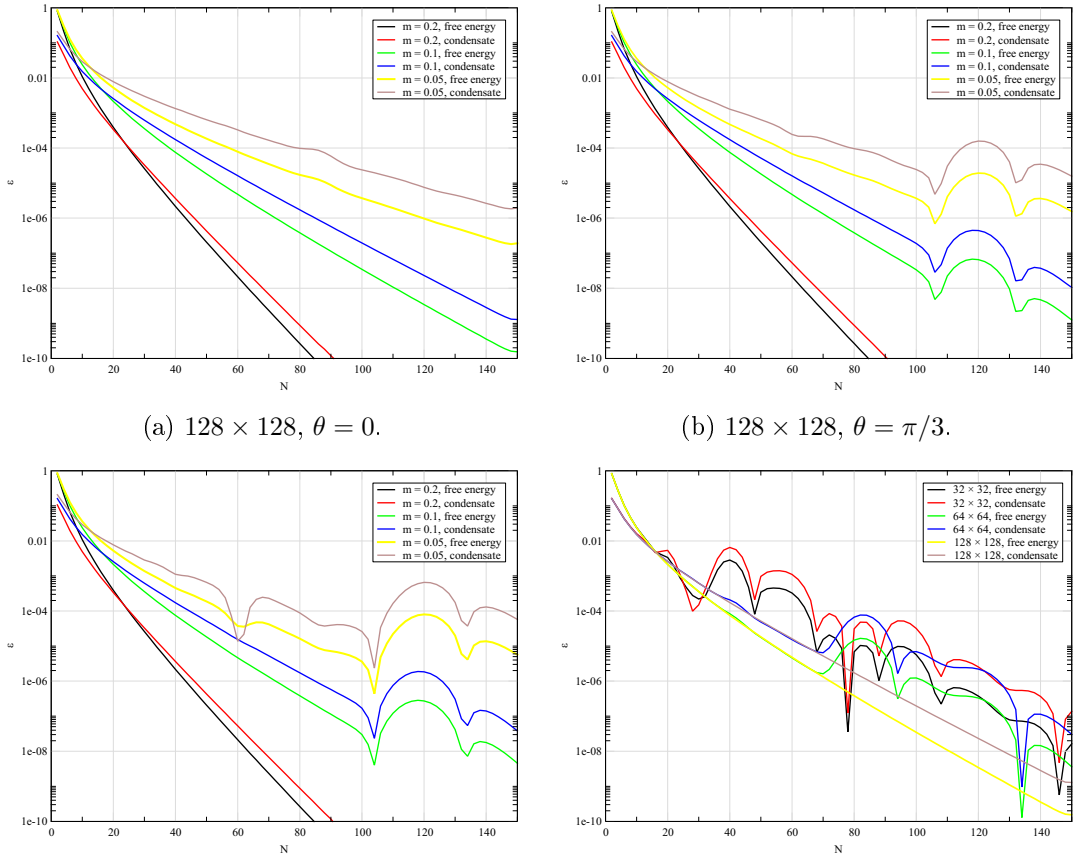

(a) 128×128, $\theta = 0$.

(b) 128×128, $\theta = \pi/3$.

(c) 128×128, $\theta = \pi$.

(d) $m = 0.1$, $\theta = 0$.

Fig. 2: Results for the relative error ε between the analytic solution and the Chebyshev approximation of the free energy and the chiral condensate, plotted against the number of Chebyshev factors N. The varied parameters are the lattice size $N_1 \times N_2$, the mass m and the imaginary chemical potential θ.

see also Fig. 1a. This explains the different convergence rates for the different masses.

What can also be seen in Fig. 2a for $m = 0.05$ at around $N = 80$ are slight instabilities of the approximation. These instabilities become much more pronounced in Fig. 2b with an increased imaginary chemical potential of $\theta = \frac{\pi}{3}$ and even more so in Fig. 2c where $\theta = \pi$. We do not concern ourselves with a detailed analysis of these irregularities. We will, however, explain shortly what seems to cause them and how they might be compensated.

Firstly, it is important to note that larger masses suppress these instabilities. For $m = 0.2$, for example, none can be seen in the displayed regions of ε and N. Secondly, an important factor for these irregularities are the positions of the eigenvalues relative to the positions of the parameters z_j on the surrounding circle. This can be seen by the fact that increasing θ only shifts the eigenvalues within the spectrum, see Fig. 1b, but

can have a strong influence on the quality of the approximation, evident in Fig. 2. What is also interesting is that for larger masses the convergence is not really affected by the change of θ up to some value of N. Looking at $m = 0.1$, for example, it is clear that the convergence is the same for all θ up to about $N = 100$. Thirdly, what can be seen in Fig. 2d, where only the lattice sizes are varied, is that the instabilities are reduced for larger lattices. This shows that the convergence is more stable when the spectrum is more densely populated. Lastly, we want to mention what is also discussed in [15], namely that the convergence of the Chebyshev approximation does not only depend on the spectrum of the matrix, but also on the parameters d and c. Therefore the approximation might also be improved by changing the position or the form of the ellipse described by the z_j in Eq. (43).

What we also need to address at this point is how well the Chebyshev factorization can approximate the determinant of the complete Dirac operator. The problem hereby is that tests like this, where we can compare the Chebyshev approximation with exact analytic results, are only possible in the free case of the theory, as we already mentioned. However, since we know how the spectrum of the free Dirac operator changes when reintroducing the gauge links, we can convince ourselves that the Chebyshev factorization with the parameters determined here also gives good approximations for the full Dirac determinant.

For this, two factors are important. The first thing to note is that the introduction of the gauge links leads to a contraction of the spectrum. This has therefore a similar effect on the convergence as increasing the mass does, since a contraction means that the spectral gap becomes larger. The second important fact is that the complete Dirac operator has less degeneracies of eigenvalues than the free operator, which means that the spectrum becomes more densely populated. This should reduce the instabilities, as it does when increasing the lattice size, see Fig. 2d. We can therefore expect the Chebyshev factorization to approximate the Dirac determinant in the interacting theory with at least comparable quality as it does in the free case.

The discussion of these results shows that finding the best parameters for the Chebyshev approximation is not a simple task, since the convergence is dependent on multiple variables. To get a more detailed understanding would require a more in-depth analysis of the Chebyshev factorization and its convergence rate. For our purposes, however, we already have enough information, since we were able to show that increasing the mass of the fermions guarantees a better convergence and also suppresses the instabilities. Especially for masses $m \geq 0.2$ it is clear that only about 100 Chebyshev factors are needed to obtain a very good agreement with the analytic solution of the free Dirac determinant. Additionally, we also argued why we expect the error for the approximation of the complete Dirac determinant to be very similar to the error of the free case.

So far we only used the Chebyshev factorization to represent the free Dirac determinant as a product of inverse determinants, which we then still calculated analytically. In the following section, however, we will approximate the free Dirac determinant without any analytical input.

5.3. Monte Carlo Simulation of the Chiral Condensate

In this section we first discuss the implementation of the Monte Carlo simulation for the chiral condensate. The expression we implement is given by Eq. (63) and Eq. (64). Following that, we discuss the results of this simulation.

5.3.1. Implementation of the Monte Carlo Simulation

The general idea of how we implement Monte Carlo simulations is summarized in Appendix A.3. Therefore, in this section, we will only need to talk about the details which are specific for the implementation of the chiral condensate, which are the action of this theory and the update procedure for the fields.

The first thing which is important to mention for Monte Carlo simulations is the action of the theory, which for the chiral condensate is given by $S_{cc}[\phi] = \sum_{j=1}^{N/2} \phi^{(j)\dagger} D_j^\dagger D_j \phi^{(j)}$, as can be seen in Eq. (64). We therefore know that we need to generate configurations of the fields ϕ which follow the distribution $\frac{e^{-S_{cc}[\phi]}}{Z}$. Also, we have to keep in mind that the fields actually carry several indices, namely n, α and j, denoting the lattice site, the Dirac component and the Chebyshev factors, respectively. Color does not contribute here since we are working with the free theory.

We now turn to the actual implementation of the Monte Carlo simulation. For this we will shortly discuss all the steps also outlined in Appendix A.3. For the cold start initialization we set all entries of ϕ equal to zero. The update sweeps over the fields were implemented by iterating over all indices of ϕ, where at each step we generated the trial configuration (cf. Eq. (A.6)) by adding a small complex number $\delta = \delta_1 + i\delta_2$ to the field, where δ_1 and δ_2 are real and random. The proposed change can therefore be expressed as

$$\phi'^{(j_0)}_{\alpha_0}(n_0) = \phi^{(j_0)}_{\alpha_0}(n_0) + \delta. \tag{65}$$

The bound for the random numbers δ_1 and δ_2 was determined by the acceptance rate of the proposed configurations, as discussed in the appendix.

To determine if this proposed change is accepted, we calculate the change of the action as given in Eq. (A.7). Since the field only changed locally, it is not necessary to calculate the action explicitly, as mentioned in the appendix. For example, since the field is only varied for a fixed value of j, the sum over the Chebyshev factors drops out when calculating the difference of the actions. Similar arguments also hold for the other pa-

rameters. This fact was of course considered when implementing the algorithm to reduce the numerical cost of evaluating the Metropolis weight in Eq. (A.8). Additionally, when calculating ΔS, it is important to keep in mind that the fields representing fermion degrees of freedom, which in this case are the pseudofermions ϕ, have antiperiodic boundary conditions in time direction, as given in Eq. (23).

The observable which needs to be calculated in this simulation is the sum within the angle brackets in Eq. (64), which can immediately be combined with the prefactors to obtain a measurement of the chiral condensate. The error of the data set was then calculated using data blocking together with the Jackknife method, as it is explained in Appendix A.3.

This concludes the discussion of the implementation of the Monte Carlo simulation for the chiral condensate. In the next section we first are going to discuss the values of all the parameters we used in the simulation and then we show the results of the calculation and compare them to the analytic result. Also we will talk shortly about how the size of the error bars was determined.

5.3.2. Monte Carlo Results for the Chiral Condensate

Before we go into detail about the numerical results for the chiral condensate, we first need to address the values of the parameters of the simulation. The lattice size was chosen to be 4×4, since that will also be the size we will use in later chapters where we implement this ansatz for the calculation of the canonical density of states. These simulations, discussed in the following chapters, are much more costly in computer time, so we could only test them with this small lattice. The number of Chebyshev factors was set to $N = 100$, since we know from Section 5.2 that this amount yields already a good approximation, especially for larger masses. For equilibration we used $n_{equi} = 2 \times 10^3$ steps, since after this amount of sweeps the configuration of the field has already reached an equilibrium, which was verified by looking at the results of the measurements of the observable. For decorrelation of the measurements $n_{skip} = 10$ sweeps were used and the number of measurements was set to $n_{meas} = 2\times10^6$. For this fixed parameter set several calculations were performed for different combinations of the remaining parameters, namely the mass m of the fermion and the imaginary chemical potential θ. The results of these Monte Carlo simulations can be seen in Fig. 3, where they are plotted together with the analytic results of the chiral condensate.

The plot clearly shows that the results have the same dependence on the parameters m and θ as we already found in Fig. 2. For small masses the error bars are relatively large but decrease steadily for increasing m, which we expected due to the behavior of the spectral gap. Also, when comparing the results for $\theta = 0$ to those with higher imaginary chemical potential, it can be seen that an increasing θ also increases the error. Again,

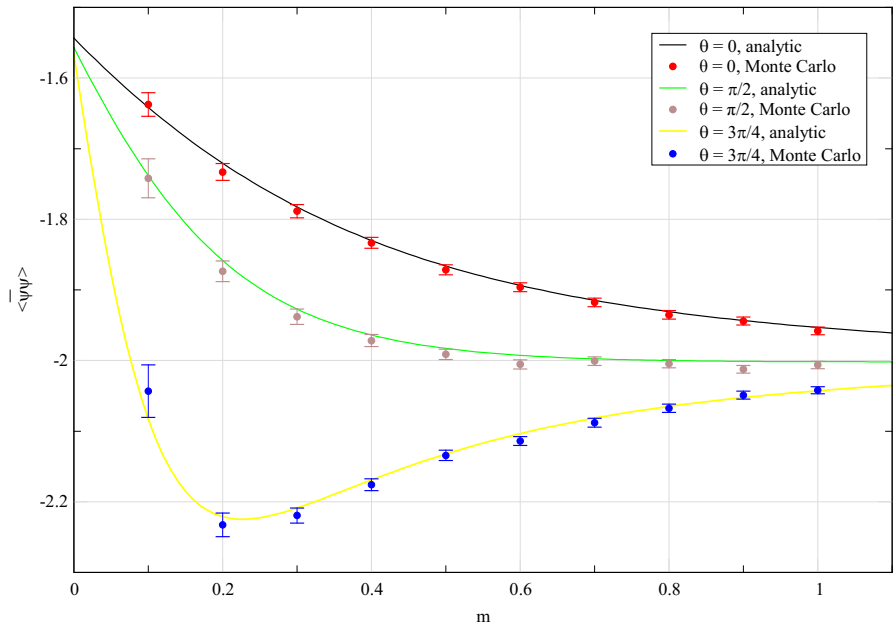

Fig. 3: Results of the chiral condensate for three different values of the imaginary chemical potential. The continuous lines are the analytic solutions and the dots represent the results of the Monte Carlo simulations, calculated on an 4×4 lattice for $N = 100$ Chebyshev factors.

this is most pronounced for small masses but can be neglected for larger m. This reflects very well the findings of the previous section.

We also want to go into a little more detail about the calculation of the errorbars for the Monte Carlo results. As mentioned in the appendix, the error was estimated using Eq. (A.10), where the criterion we used to fix the number of elements per blocks n is also discussed there. In Fig. 4 we show how the error σ behaves for an increasing size of the data blocks for the Monte Carlo simulation of the chiral condensate with an imaginary chemical potential of $\theta = \frac{3\pi}{4}$. As can be seen, for higher values of n the errors almost reach a constant value, where for smaller masses larger blocks are necessary for this to happen. Also, we want to stress at this point that the lines connecting the results in the figure are of course only a guide to the eye an do not represent actual numerical results. The size of the blocks used for the result in Fig. 3 is $n = 5^6 = 15625$.

With this we can conclude this chapter about the first numerical tests of the Chebyshev factorization and the pseudofermion representation. We were able to show that for masses larger than $m = 0.2$ the Chebyshev approximation already yields satisfying results for $N = 100$ factors and all values of the imaginary chemical potential. Also, the results of the Monte Carlo implementation of the chiral condensate show that good approximations can be achieved for the multi-boson representation of the free Dirac determinant,

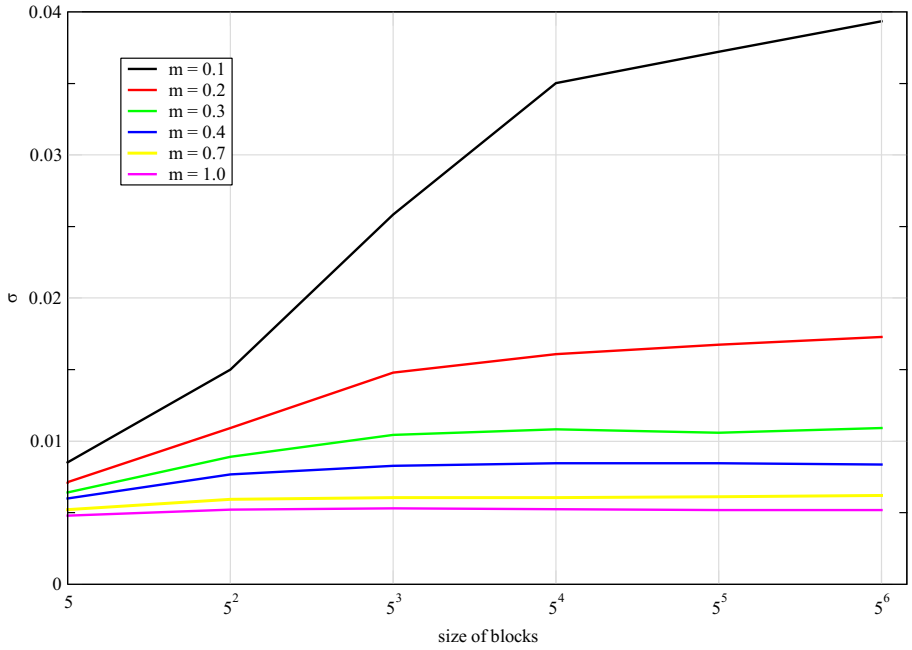

Fig. 4: Behavior of the error estimation for the chiral condensate when different sizes of the blocks are used for the Jackknife method. Here, the error for $\theta = \frac{3\pi}{4}$ is shown for several values of the mass m. The lines connecting the data points are only a guide to the eye.

especially if the value of the mass is not too small. What we also discussed was that although we only tested the free case, we can expect the Chebyshev factorization ansatz to also give results of a similar quality for the interacting theory. In the next chapters we will use the same Monte Carlo methods to calculate the restricted expectation value via the FFA approach, which will enable us to calculate the density of states.

6. Testing the FFA for the Free Theory

Before we go into detail about the implementation of the functional fit approach (FFA), we want to recapitulate the steps we took in the last two sections. There we described and tested two methods which we need for an efficient implementation of the Dirac determinant, which is a central quantity of the restricted expectation values, which in turn is needed for the FFA. The two methods are of course the Chebyshev factorization of the determinant which, combined with the pseudofermion ansatz, leads to the multi-boson representation of the Dirac determinant. We verified their applicability for our theory by looking at the behavior of the eigenvalues of the Dirac operator. Following that, in the subsequent chapter, we introduced two quantities for numerical testing of these methods. First, in Section 5.2, we explicitly tested only the Chebyshev factorization, and then in Section 5.3 we also included the pseudofermions and tested the complete ansatz with Monte Carlo simulations. After all this we concluded that this is a valid method for approximating the Dirac determinant, so that we can now proceed to use it for the implementation of the FFA.

In the first section of this chapter we will discuss how the density of states and the restricted expectation values look like for the free theory and also go into the details of the Monte Carlo simulation of the FFA. Following that, in the second section, we present our numerical results and compare them to the analytic solution.

6.1. Implementation of the FFA for the Free Theory

In this chapter, we will test the FFA as it is presented in Section 3.3, although we will still stay with the free case so that we are able to verify our results with the analytic solutions. Additionally, we will also only consider the case where the observable is set equal to unity, $\mathcal{J} = \mathbb{1}$. As discussed when introducing the density of states method, this corresponds to the density which is needed to calculate the normalization, as can be seen in Eq. (27). It is therefore a central quantity, since it is essential for the calculation of any observable with this method. Finally, as was also the case in the previous chapters, it is sufficient if we work with only a single quark flavor.

The density which we aim to calculate in this chapter can thus be expressed via Eq. (26), where we can just apply the above mentioned simplifications. This leads to the relatively simple density

$$\rho^{(\mathbb{1})}(\theta) = \det D\left(\mu\right)\Big|_{\mu=\frac{i\theta}{\beta}}, \tag{66}$$

where all the contributions of the gauge links just drop out in the free theory, as we discussed already in an earlier chapter. It is clear that the right hand side of this equation can be calculated analytically with Fourier transformation as before. Also what is easy

to see here, is that if we introduced a second flavor where the quarks have the same mass, we would only need to square the result we obtain for the density.

For the numerical calculation of the density we will employ Monte Carlo simulations to compute the restricted expectation values from Eq. (33). Here, we now also need to express the Dirac determinant via the multi-boson representation as given in Eq. (50), where the sum over the Chebyshev factors in the exponent only needs to go up to $N/2$ since we work with just a single flavor. Additionally, instead of writing the sum explicitly, we will use the shorthand notation $\sum_{j=1}^{N/2} {\phi^{(j)}}^\dagger D_j^\dagger D_j \phi^{(j)} = \phi^\dagger D^\dagger D \phi$. Finally, when also using the same simplifications as before, we see that the restricted expectation value for the partition function of the non-interacting theory is given by

$$\begin{aligned} \langle\theta\rangle_n^{(\mathbb{1})}(\lambda) &= \frac{1}{Z_n^{(\mathbb{1})}(\lambda)} \int_{\theta_n}^{\theta_{n+1}} \mathrm{d}\theta \int \mathcal{D}[\phi]\, e^{-\phi^\dagger D^\dagger D \phi} e^{\lambda\theta}\theta, \\ Z_n^{(\mathbb{1})}(\lambda) &= \int_{\theta_n}^{\theta_{n+1}} \mathrm{d}\theta \int \mathcal{D}[\phi]\, e^{-\phi^\dagger D^\dagger D \phi} e^{\lambda\theta}. \end{aligned} \tag{67}$$

As a reminder we want to mention that the Dirac operator in the exponent is given by Eq. (14), where the hopping matrix H for the free theory is shown in Eq. (51). Here it is of course important to keep in mind that the hopping matrix is dependent on the imaginary chemical potential θ.

Now we will turn to discussing the Monte Carlo implementation of Eq. (67), where we only explain the details of this application since the general steps are outlined in Appendix A.3. It is clear that we now have two quantities we need to consider in our update steps: the imaginary chemical potential θ and the complex fields ϕ. These two come with different parts of the action and therefore follow different distributions. The action part for the field is given by $S_\phi = \phi^\dagger D^\dagger D \phi$, whereas for the part with θ also the dependence on the artificial parameter λ has to be considered, hence $S_\theta = \phi^\dagger D^\dagger D \phi - \lambda\theta$. For the proposed update of the two integration variables (Eq. (A.6)) we perform the small, additive variations

$$\begin{aligned} \phi'^{(j_0)}_{\alpha_0}(n_0) &= \phi^{(j_0)}_{\alpha_0}(n_0) + \delta_\phi, \\ \theta' &= \theta + \delta_\theta. \end{aligned} \tag{68}$$

The update for the field $\delta_\phi = \delta_1 + i\delta_2$ is here precisely the same as in Eq. (65), where for a complete sweep we had to loop over all indices. For θ however, since it is just a real valued parameter, the update is simply given by a small and random real number δ_θ. Here it is of course important to remember that the θ integration is confined to the n-th subinterval. This gives rise to different possibilities for how this update should be implemented. We tested two different versions and will compare the results in the next section. For Version 1, if the suggested new value θ' lies outside the allowed bounds, we disregard this configuration and immediately create a new one. This is iterated until a

valid value is found. For Version 2, however, if θ' lies outside the allowed integration range it is disregarded and the Monte Carlo simulation proceeds without changing θ in the current sweep.

If a possible configuration for either of the variables was found, the change in action was calculated via Eq. (A.7), using S_θ for the imaginary chemical potential and S_ϕ for the fields, and then accepted with the probability Eq. (A.8). To reduce the numerical cost when calculating the change of the actions, the locality of the update was considered here in the same way as also mentioned in Section 5.3.1. The update of θ, on the other hand, is not locally restricted, but contributes on every lattice site in time direction, see Eq. (51), which makes the evaluation of ΔS_θ rather expensive, compared to a single update of a pseudofermion field.

The bounds for the random numbers were again determined by the acceptance rates for the proposed updates of the variables. As explained in the appendix, a desired acceptance rate would be around 0.5. For the update of the imaginary chemical potential, however, we settled for an acceptance of around 0.9, which indicates that the variation is actually rather small. This does not pose a problem, however, since the reason for this is only the fact that the allowed intervals $[\theta_n, \theta_{n+1}]$ are small. So increasing the size of the variation δ_θ would only lead to more suggested updates θ' out of bound. This tells us that although the variation is small, we still can easily cover the whole integration range, which is true regardless of which of the two update versions is used.

What we also need to address for the Monte Carlo implementation of restricted expectation values is the fact that we have to implement integrations over the two different variables θ and ϕ. This raises the question in what order the updates should be performed, for example if θ should be updated more often than just once per sweep. To explore this, we tested two different update methods with short test runs of the simulation. For the first method we suggested an update for θ after every complete update of one Chebyshev field $\phi^{(j)}$. This means that in every sweep a total of $N/2$ updates for θ were suggested. For the second method we just updated the imaginary chemical potential once per sweep after all Monte Carlo steps for ϕ were done. We found that the two procedures yield very similar results. Therefore the obvious choice was to use method two for further calculations, since it requires much less numerical effort. Especially because the update of θ is not local, as mentioned above.

What we also need to mention is the evaluation of the observable of the restricted expectation values. As can be seen in Eq. (67), for example, the observable is just given by the imaginary chemical potential. So the determination of the observable here is particularly simple, since all that needs to be done for a measurement is to save the current value of θ into a file.

Finally, before we can talk about the values used for all of the parameters in the

simulation, we need to specifically address the parameter λ to find out what values are appropriate for this quantity. To do that, we first want to recapitulate where this parameter originates. It was introduced as an artificial parameter in the definition of the restricted expectation values in Eq. (33). Since it is a real parameter which effectively just substitutes the imaginary unit in the Fourier factor in Eq. (25), it removes the complex action problem and makes Monte Carlo methods accessible. The idea of the FFA is then to perform several calculations of the restricted expectation values in every interval I_n from Eq. (28) for different values of the parameter λ to get data sets which can be used to fit the function h of Eq. (38).

The question which obviously arises at this point is what values of λ are adequate for this procedure. This can be answered when first looking at Eq. (37). Here it can be seen that the argument s of $h(s)$ has the simple dependence $s \propto \lambda - k_n^{(\mathcal{J})}$, where $k_n^{(\mathcal{J})}$, the slope of the density in the interval I_n, is the quantity we aim to find with the fit. Secondly, we also know that the function has its only root at the origin, $h(0) = 0$, as stated in Eq. (39). Therefore, if we interpret h as a function of λ, all that the fit entails is finding the function's root, which is given at the position $\lambda = k_n^{(\mathcal{J})}$. Consequently, the best choices for λ are near the root to minimize the error in the fitting procedure.

Naturally, the exact position of the root is unknown. It can be estimated, however, with preliminary calculations which are called preconditioning. In this procedure crude calculations of the restricted expectation values are performed for some guessed values of λ to find a first estimate for the root. With this information one can then adjust the values of λ accordingly, so that for the full run of the calculation optimal choices can be implemented.

This form of preconditioning is not necessary for the simple case we discuss in this chapter, however. Since we are working with the case where the observable is set to $\mathcal{J} = \mathbb{1}$ and where there is no interaction between the (pseudo-)fermions, we can calculate the slope $k_n^{(\mathbb{1})}$ of the density of states and therefore the root of h explicitly. This can easily be seen via (here $\theta \in I_n$)

$$\frac{\partial}{\partial\theta} \ln\left(\det D\right) = \frac{\partial}{\partial\theta} \ln\left(\rho^{(\mathbb{1})}(\theta)\right) = \frac{\partial}{\partial\theta} \ln\left(A_n^{(\mathbb{1})} e^{-\theta k_n^{(\mathbb{1})}}\right) = -k_n^{(\mathbb{1})}, \tag{69}$$

where for the first step we employed Eq. (66) and then we could make use of the ansatz for the density, given in Eq. (32). The left hand side can easily be calculated with Eq. (58) where $s = 1$, since the derivative can be obtained by a straightforward calculation. Also it is clear that in order to get an estimate for the slope in the n-th interval one has to choose $\theta \in I_n$.

With this we have discussed all the important aspects for the Monte Carlo implementation of the FFA for the free theory. In the next section we will first fix all the values of

the parameters which are still left open. After that we will show plots where we compare our numerical results with the analytic solution. Also we discuss in detail the fitting procedure for the slopes of the density.

6.2. Numerical Results for the Free Density of States

Before we can present our numerical results, we first need to mention all the values of the parameters included in the simulation. Two important quantities, which need to be chosen with care, are the number of subintervals for the θ integration, N_θ, and also the number of values for the parameter λ, which we call N_λ. The first one regulates with how many intervals the density is discretized, which is of course an important aspect of the density of states ansatz. One has to keep in mind that a rather precise description of $\rho^{(\mathbb{1})}$ is needed for the evaluation of the Fourier integral in Eq. (27). On the other hand, also the numerical effort has to be considered. Therefore, similar to the procedure for finding the best values for λ, one can perform preconditioning runs to first get a crude approximation for the behavior of $\rho^{(\mathbb{1})}$. This can be done with a rather low number of intervals. With this information it is then possible to choose an appropriate number N_θ for the subintervals. Additionally, what can also be made use of at this point, is the fact that the size of each subinterval Δ_n can be adjusted individually. This is a convenient method with which the accuracy in regions of fast variation of the density can be increased by choosing smaller subintervals. Alternatively, it is also possible to save computer time by enlarging the subintervals in regions where the variation is slow. For the free theory, however, this kind of preconditioning is not necessary since we can calculate the density analytically. Now, to turn our discussion back to actually setting the parameters, we chose $N_\theta = 50$ equally sized subintervals for the θ integration. The interval size is thus given by $\Delta_n = \frac{\pi}{50}$, $\forall\, n$.

The parameter N_λ has a similar influence on the quality of the approximation as N_θ does. If more calculations for different values of λ are performed in each subinterval I_n, then the errors made in the fit of the function h are reduced. But the number of calculations for λ can not be set too high since this is also numerically very expensive. With this in mind we chose for our calculations $N_\lambda = 7$. In combination with the number of subintervals this means that for the full calculation of the density a total of $N_\theta N_\lambda = 350$ Monte Carlo simulations have to be performed. For the actual values of λ we estimated the slopes with the analytic result of Eq. (69) for some $\theta \in I_n$ and chose the seven values equally spaced within $[k_n^{(\mathbb{1})} - 1, k_n^{(\mathbb{1})} + 1]$.

For the remaining parameters we chose very similar values as we did in Section 5.3.2. The number of Chebyshev factors was set to $N = 100$ since the results with this amount were satisfying for the tests we did in the last chapter. Also the lattice size was again set to 4×4. For the mass of the fermions we used the value $m = 0.5$, since at this point

no strong θ-dependence in the error can be seen in the results of Fig. 3. Finally, we also need to mention the Monte Carlo parameters. For the equilibration of the configurations of the fields we used $n_{equi} = 10^4$ and for the decorrelation between the measurements $n_{skip} = 10$ update sweeps were performed. The total number of measurements used in the simulation was $n_{meas} = 10^7$. Now that we discussed the values of all parameters in our simulation, we can proceed to showing the results of the calculations.

First, we have to return to the previously mentioned fact that we explored two different versions for the update of the θ variable in the Monte Carlo simulation. What we found when comparing the normalized restricted expectation values for the two versions, which are explained later on, is that the results for Version 1 do not agree as well with the fitting function h. The reason for this can be seen when comparing the distribution of the θ measurements within one subinterval, which is done in Fig. 5 for the interval $n = 0$ and $\lambda = 1$. Due to the exponential factor $e^{\lambda\theta}$ in the integral Eq. (67), the distribution should be roughly of exponential form[9]. While this is true for Version 2 of the update, as can be seen in the right plot, Version 1 yields a distorted distribution.

Why this happens can be understood in the following way: Version 1 forces θ to find a possible configuration within the given interval. But if the current value of θ is already near the edge, the only possible update is a jump away from that edge. Also, since the acceptance rate in the Metropolis step is high, these jumps are accepted most of the time. This pushes the values for θ away from the edges, as can be seen on the left hand side of Fig. 5. With Version 2, this cannot happen, since if an out-of-bound value is suggested, θ simply does not change. This allows more configurations where θ is close to the edge. Therefore, for all following calculations, we only use Version 2 of the update, since this yields much smoother distributions of θ and more consistent results.

Now that we also decided on the update version for the θ integration, we can show the results for the restricted expectation values. In Fig. 6, the results after normalization via Eq. (37) for a selection of subintervals n are plotted. The symbols in this plot show the results of the Monte Carlo simulation, where the errors were again calculated using the Jackknife method. The continuous lines are the fits of the linearized version of the function h from Eq. (38) to the numerical results, as explained below. The λ values where the lines cross the origin give the slope $k_n^{(\mathbb{1})}$ for the density $\rho^{(\mathbb{1})}$ in the interval n. As can be seen, the slope starts at around zero for the first subinterval $n = 0$ and then increases up to $n = 30$. Afterwards, the slope reduces and ends up at around zero again for the last subinterval $n = 49$.

As we just mentioned, the function used to fit the data is not actually the full function stated in Eq. (38), but a linearized version which will be denoted by $\widetilde{h}$. The reason we use the linearization is given by the fact that the fitting procedure becomes much simpler

[9]Whether the distribution increases or decreases depends on whether $\lambda > k_n^{(\mathbb{1})}$ or $\lambda < k_n^{(\mathbb{1})}$, respectively.

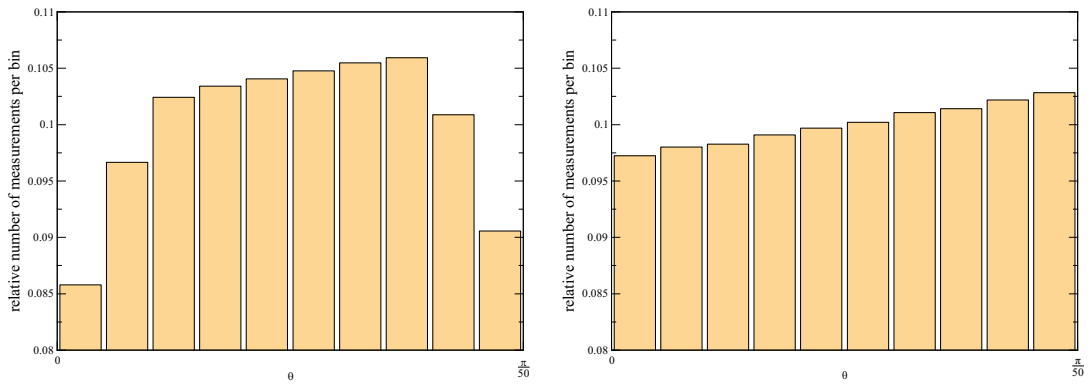

Fig. 5: Distribution of the measurements of the imaginary chemical potential θ within the first subinterval $n = 0$ with $\lambda = 1$ for the two different update methods in the Monte Carlo simulation. Left is the result of the method we called Version 1, right is Version 2.

this way, while the agreement between the linear function and h is still very good in the region of interest. To calculate $\widetilde{h}$ we express the actual function using the Taylor series, which is given by

$$h(s) = h(0) + h'(s)\big|_{s=0}\, s + \mathcal{O}\big(s^2\big)\,.$$

Inserting here the properties of h stated in Eq. (39) and ignoring contributions of order $\mathcal{O}\big(s^2\big)$, it is easy to see that the linearized function can be written as

$$\widetilde{h}\left(\Delta_n\left[\lambda - k_n^{(\mathbb{1})}\right]\right) = \frac{\Delta_n}{12}\left(\lambda - k_n^{(\mathbb{1})}\right). \tag{70}$$

Since we now already made use of the fact that the slope of the function h at the origin is given analytically, the fit using the linear function reduces again to a simple one-parameter fit.

For completeness of the argument, we also want to mention how big the error between h and $\widetilde{h}$ is in the region of interest. Since we centered the values for λ around the analytic result of the slope, the maximal value of the argument of the functions can be $s \approx \pm\Delta_n$, which gives an absolute error of about $\varepsilon = \left|\widetilde{h}(s) - h(s)\right| \approx 3.5 \times 10^{-7}$. The linearization is therefore clearly an acceptable approximation, especially when considering the size of the errorbars in Fig. 6. Also, this plot gives an important consistency check for our calculations, since it shows that the slopes of the restricted expectation values agree very well with the analytical value of $\frac{\Delta_n}{12}$ as given in Eq. (39). For Version 1 of the θ update this slope would be slightly underestimated, due to skewed distribution of Fig. 5.

The next step is now to use the slopes $k_n^{(\mathbb{1})}$, which were obtained by the linear fit of

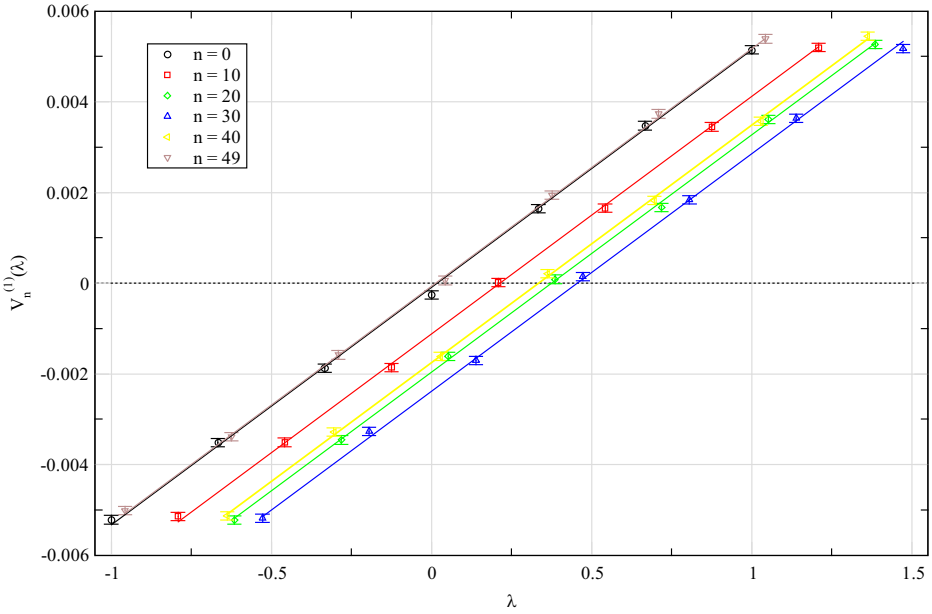

Fig. 6: Results for the normalized restricted expectation values plotted over the parameter λ for the non-interacting theory. The lines depict the linear fits of the data in the same color. The Monte Carlo simulation was performed on a 4×4 lattice with $N = 100$ Chebyshev factors and a fermion mass of $m = 0.5$.

the normalized restricted expectation values $V_n^{(\mathbb{1})}$, to calculate the density of states $\rho^{(\mathbb{1})}$. This can be done by inserting the slopes into Eq. (32), which yields a piecewise linear approximation of the density. The result can be seen in the left plots of Fig. 7, where also the analytic solution for the density obtained by Fourier transformation is displayed as the black line. In the plot on the right side the relative error between the analytic and numeric solution is shown. It was calculated via

$$\varepsilon_\rho(\theta) = \frac{\rho_{MC}^{(\mathbb{1})}(\theta) - \rho_{FT}^{(\mathbb{1})}(\theta)}{\rho_{FT}^{(\mathbb{1})}(\theta)}, \tag{71}$$

where $\rho_{FT}^{(\mathbb{1})}(\theta)$ denotes the analytic solution and $\rho_{MC}^{(\mathbb{1})}(\theta)$ is the result of the Monte Carlo simulation.

As can be seen, at the start of the interval, where $\theta = 0$, we have no error at all. This is of course due to the reason that we used this point to normalize the density, which enabled us to express it in terms of only the slopes. Then, for an increased imaginary chemical potential, the numerical results are slightly lower than the analytical solution up to about $\theta = \frac{\pi}{4}$. After this point the Monte Carlo simulation yields too high values for $\rho^{(\mathbb{1})}(\theta)$ and the error increases until $\theta = \pi$. To understand this, it is important to keep in mind that the value of the density in one subinterval n is also dependent on all

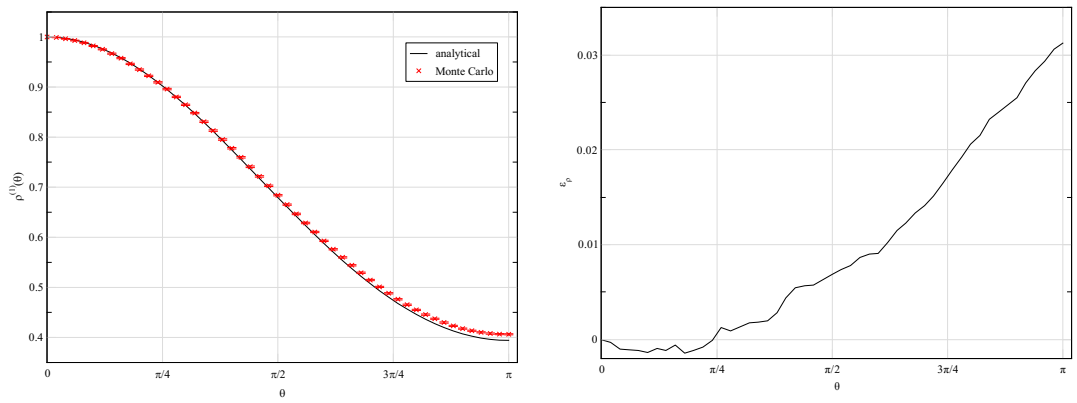

Fig. 7: Results for the Monte Carlo simulation of the density of states $\rho^{(\mathbb{1})}(\theta)$ for the non-interacting theory. On the left-hand side, the comparison to the analytic solution can be seen, and on the right the relative error ε_ρ is plotted. The Monte Carlo simulation was performed on a 4×4 lattice with $N = 100$ Chebyshev factors and a fermion mass of $m = 0.5$.

previous slopes k_n, $n = 0, \ldots, n-1$, as can be seen in Eq. (31). Therefore an error for one slope also influences the approximation of $\rho^{(\mathbb{1})}(\theta)$ for all following subintervals. So the behavior of the error indicates that the approximated slopes for the subintervals are mostly underestimated. Also it needs to be mentioned that the error again was calculated using the Jackknife method but is still underestimated, as can be seen in the left plot of Fig. 7.

Finally, we can summarize this chapter by stating that we found that it is sufficient to use a linear function to fit the slope and also that the slopes of the normalized restricted expectation values do agree very well with the expected analytic values. Nevertheless, we found that the slope of the density tends to be underestimated, which results in larger errors for higher values of the imaginary chemical potential. We do want to stress, however, that there are still several ways with which this density of states method may be improved. Some of these are discussed at the end of the next chapter, after we tested this method for full QCD which includes the SU(3) dynamics of the gauge links.

7. Application of the FFA to Full QCD

In this chapter we will use the FFA to calculate the density of states for the full theory of QCD. The structure of this chapter is in essence the same as the previous one for the free theory. Firstly, we will repeat all the expression which are important for the implementation of the FFA, namely the density and the restricted expectation values, and we will discuss the update procedure for the Monte Carlo simulation, where we need to focus especially on the role the SU(3) structure has, since this is the defining difference to the last chapter. Following that, in the second section, we will show and discuss the numerical results. Finally, in the last section, we discuss the numerical implementation of the theory and the consistency of the results more generally, and we will also look at possible improvements for future applications of the density of states method.

7.1. Implementation of the FFA for the Full Theory

At first, it is of course important to look at the density which we aim to calculate. As in the previous section, we are only interested in the case where the observable is set equal to unity, $\mathcal{J} = \mathbb{1}$. Again, this corresponds to the density which is needed for evaluating the normalization in Eq. (27). Other than that, no further simplifications are possible at this point. Therefore, with Eq. (26), it is easy to see that the density we are working with in this chapter is given by

$$\rho^{(\mathbb{1})}(\theta) = \int \mathcal{D}[U]\, e^{-S_G[U]} \det{}^2 D\,[U,\mu]\,\Big|_{\mu=\frac{i\theta}{\beta}}. \tag{72}$$

In contrast to all previous calculations, we now consider two mass-degenerate flavors explicitly in the gauge link integral.

To calculate this density, we of course want to employ the FFA and therefore need to calculate the restricted expectation values using Monte Carlo simulations. In order to do that, we express the the squared determinant using the multi-boson representation as given in Eq. (48). Similar to the previous chapter, we introduce a shorthand notation for the exponent and write $\sum_{j=1}^{N} {\phi^{(j)}}^\dagger D_j^\dagger D_j \phi^{(j)} = \phi^\dagger D^\dagger D \phi$, where the sum now includes N terms since we have two flavors. The expectation values to calculate, given by Eq. (33), can thus be expressed as

$$\begin{aligned} \langle\theta\rangle_n^{(\mathbb{1})}(\lambda) &= \frac{1}{Z_n^{(\mathbb{1})}(\lambda)} \int_{\theta_n}^{\theta_{n+1}} \mathrm{d}\theta \int \mathcal{D}[U] \int \mathcal{D}[\phi]\, e^{-S_G[U]} e^{-\phi^\dagger D^\dagger D \phi} e^{\lambda\theta}\theta, \\ Z_n^{(\mathbb{1})}(\lambda) &= \int_{\theta_n}^{\theta_{n+1}} \mathrm{d}\theta \int \mathcal{D}[U] \int \mathcal{D}[\phi]\, e^{-S_G[U]} e^{-\phi^\dagger D^\dagger D \phi} e^{\lambda\theta}. \end{aligned} \tag{73}$$

Here we want to remind the reader that the Dirac operator $D\,[U,\theta]$ is in fact a functional

of the gauge links U and is also dependent on the imaginary chemical potential θ. Its exact form is given in Eq. (14). The hopping matrix is shown in Eq. (21), where the substitution $\mu = \frac{i\theta}{\beta}$ still has to be performed. The expression used for S_G is the Wilson gauge action which is given in Eq. (10).

For the Monte Carlo implementation it is now again important to look at the action of the theory. As before, the different variables come with different parts of the action and therefore follow different distributions. For the fields ϕ and U and the variable θ the different parts are given by

$$\begin{aligned} S_\phi &= \phi^\dagger D^\dagger D\phi, \\ S_U &= S_G + \phi^\dagger D^\dagger D\phi, \\ S_\theta &= \phi^\dagger D^\dagger D\phi - \lambda\theta, \end{aligned} \tag{74}$$

respectively. It can be seen that S_ϕ and S_θ are structurally still the same as in the free theory. As before, it is important to discuss the update procedure of the different variables in the Monte Carlo simulation. The variations we perform in the calculation can be written as

$$\begin{aligned} \boldsymbol{\phi}'^{(j_0)}_{\alpha_0}(n_0) &= \boldsymbol{\phi}^{(j_0)}_{\alpha_0}(n_0) + \boldsymbol{\delta}_\phi, \\ U'_{\nu_0}(n_0) &= XU_{\nu_0}(n_0), \\ \theta' &= \theta + \delta_\theta, \end{aligned} \tag{75}$$

where X is an SU(3) matrix in the vicinity of $\mathbb{1}$.

By far the simplest update of these three is the one for θ, which is exactly the same as in the previous chapter and consists just of a small real and random number δ_θ. Also, the update for the pseudofermion fields works with the same principle as before, but with one very important difference. Since we are working now with the full theory, the fermion fields gained an additional degree of freedom which describes the interaction with the SU(3) gauge links. Therefore the fields $\boldsymbol{\phi}$ as well as the variation $\boldsymbol{\delta}_\phi$ in Eq. (75) are three dimensional color vectors, were the entries of the variation vector are again small and random complex numbers. So each entry of the vector equation effectively follows the same update step as in Eq. (68). Alternatively, instead of using vectors to update all the color components in one step, it would of course also be possible to update each color entry separately as it is done for the components of the Dirac space, for example.

Now we turn our attention to the newly introduced update for the gauge links. A defining difference is here that the change in configuration is not achieved by an additive but a multiplicative variation of the links. This is of course due to the fact that the U are elements of the SU(3) gauge group and we need to make sure that this structure is

preserved. The small variation can therefore be described with an SU(3) matrix X, which is generated in a way such that the product XU modifies the matrix U only slightly. This can be achieved if X is close to the unit element of the group, which is of course simply the 3×3 identity matrix. To understand how this X can be generated, we shortly discuss in general terms how SU(3) matrices can be constructed in the first place.

Given the properties of SU(3), namely unitarity and unit determinant, it is possible to construct these matrices by first generating two random complex vectors $\mathbf{u}$ and $\mathbf{v}$, which represent the first two columns of a matrix. These vectors have to be orthogonal, which can be achieved for example by using the Gram-Schmidt process, and also normalized. The last column can then be calculated via a cross-product of the first two, accompanied with a complex conjugation. General SU(3) matrices can therefore be expressed as

$$U = (\mathbf{u}, \mathbf{v}, (\mathbf{u} \times \mathbf{v})^*)\,. \tag{76}$$

It can be verified that matrices of this form really are elements of SU(3) by checking $U^{-1} = U^\dagger$ and $\det U = 1$.

Also, what we want to mention at this point, is the fact that due to the properties of SU(3) matrices, they can be fully characterized using only eight real parameters. It is, however, numerically cheaper to create them the way explained above. Also, since the last column of the matrix can be generated by the first two, one could save memory by only storing $\mathbf{u}$ and $\mathbf{v}$. But the matrices play a very dominant part in the simulation, and since speed was of far more concern than memory in our calculation, storing them explicitly was the preferred choice.

Now, for the generation of X, we can not create a fully random SU(3) matrix as outlined above, since we need to make sure that it is near the unit element. This of course means that the real diagonal entries have to be larger compared to all other entries. To achieve this, an additive real valued bias δ_U is introduced when generating the random vectors $\mathbf{u}$ and $\mathbf{v}$. To make sure that only the diagonal is influenced by this bias, one only has to alter the first and second entry of $\mathbf{u}$ and $\mathbf{v}$, respectively, via $u_1 \to u_1 + \delta_U$ and $v_2 \to v_2 + \delta_U$. This shift has of course to be performed before orthogonalization and normalization. The resulting matrix then shows the desired property of having a dominant real part on the diagonal. Since δ_U controls the magnitude of the change of the field, as it is also the case with the variation of the other variables, an appropriate value for the bias has to be determined by looking at the acceptance rate of the varied gauge links in the Metropolis step of the Monte Carlo simulation. The only difference here is that larger values of δ_U create smaller variations, whereas for $\boldsymbol{\delta}_\phi$ and δ_θ it is the other way around.

The last thing we need to address regarding the update of the gauge links is the problem of numerical error. It is clear that the matrices in our simulation are just approximations of SU(3) elements due to their finite precision. This fact does not pose a problem in itself

since the error is small enough. However, during the repeated multiplications of these matrices in the updating process the error accumulates and the matrices drift further and further away from the needed SU(3) structure. If many sweeps are performed in the simulation, this will influence the quality of the results significantly. To combat this, normalization updates have to be performed periodically, where the gauge links are projected back into the group. This can be achieved by orthogonalizing and normalizing the first two columns and then calculating the third one as shown in Eq. (76). The frequency with which this normalization is performed is a new parameter in the Monte Carlo simulation, which we call n_{repro}. Also we want to mention that for the initialization of the gauge links in the Monte Carlo simulation, using a cold start, we set the links to $U_\nu(n) = \mathbb{1},\ \forall\, \nu, n$.

After this specific discussion of the SU(3) update, we can summarize the remaining steps in general terms, since they are the same for all variables. If a possible configuration was found, we followed again the procedure outlined in the appendix, where we calculate the change of the corresponding part of the action via Eq. (A.7) and accept the new configuration with the probability Eq. (A.8). Here it is of course also possible to experiment with different update orders for the fields in the simulation. An example of this was discussed in the last chapter. The way we implemented the sweep for the current case is just by updating one field after the other. So we first suggested variations for all degrees of freedom in $\boldsymbol{\phi}$, followed by a sweep over n and ν for U and finally varied the imaginary chemical potential θ. Performing a measurement of the observable of the restricted expectation value is again simply given by saving the current value of θ.

In next section we will discuss the numerical results for this implementation. As usual, we begin with listing the values of all the parameters and then show and discuss the results in detail. Also, in the subsequent section, we review our implementation of the theory and also introduce a fitting procedure which can be important for future applications of the FFA.

7.2. Numerical Results for the Full Density of States

For the testing of the full theory, we will mostly use the same values for the parameters as we did for in the free case. Especially for the mass and the Chebyshev factorization this is important, since we want to ensure the same or a better approximation of the Dirac determinant. Despite the similarities of the parameters, we will still list all values here again, for the sake of completeness in this section.

Now, starting with the only parameters which can have a physical interpretation, we set the mass of the fermions to $m = 1$, which is twice the value we used in the free case to improve the numerical stability of the Chebyshev factorization. The new parameter β, the gauge coupling, which is introduced together with the gauge links since it appears

in the action Eq. (10), was set to $\beta = 6$. The size of the lattice on which the calculations were performed was 4×4, and the number of Chebyshev factors, which corresponds to the number of pseudofermion fields, was $N = 100$. The interval $[0, \pi]$ of the density was discretized into $N_\theta = 50$ equal subintervals, giving an interval size of $\Delta_n = \frac{\pi}{50}$, $\forall n$. To find the slopes of the density $\rho^{(\mathbb{1})}$ in those subintervals using the fit, we calculated the restricted expectation value Eq. (73) for $N_\lambda = 7$ different values of λ. Here, of course there exists no analytic solution to center the values of λ around. But after short preconditioning runs, it was decided to distribute the values of λ evenly around the origin within the intervals $[-1, 1]$ for all subintervals. As before, to calculate the density a total of $N_\theta N_\lambda = 350$ different Monte Carlo simulations have to be performed. Now turning to the Monte Carlo parameters, we used $n_{equi} = 2 \times 10^4$ equilibration sweeps to relax the system from the cold start. For decorrelation of the measurements, $n_{skip} = 10$ sweeps were performed, and to ensure that the gauge links stay within SU(3), they were normalized after every $n_{repro} = 5 \times 10^2$ sweeps, as discussed in the previous section. Finally, the number of measurements taken for our results was $n_{meas} = 4 \times 10^6$. The results achieved with this set of parameters are discussed below, where all errorbars were calculated using the Jackknife method Eq. (A.10).

In the following figure, Fig. 8, the results for some exemplary normalized restricted expectation values are shown, together with the fit to the linear function of Eq. (70). As already extensively discussed in the previous section, the λ value where the fit crosses the origin gives the slope of the density $\rho^{(\mathbb{1})}$ in the n-th subinterval. What can immediately be seen when comparing these results to the one for the free case in Fig. 6, is that the slopes of the density seem to be much smaller in the interacting theory, since the crossing occurs very close to the origin. In fact, this is the case for all subintervals, which means the density is very flat. This is also the reason why only three subintervals are shown in the figure, since the results for the all the other look very similar and the plot would become too crowded if more are displayed.

As for the free theory, the next step is to use the slopes $k_n^{(\mathbb{1})}$ obtained by the fit to calculate the density of states $\rho^{(\mathbb{1})}$ via Eq. (32). The result for this calculation is shown in Fig. 9. Unfortunately, however, this result does not look very promising. Based on our understanding of the non-interacting theory, we chose the values of the parameters carefully, especially regarding the mass and the number of Chebyshev factors, to yield a good convergence. Therefore, we expected the result to be much smoother and with less fluctuations. Especially the larger jumps, for example at $\theta \approx \frac{\pi}{3}$, seem rather unnatural. What can be seen nicely, however, is the fact that the error increases with increasing θ, which is expected since the error in one subinterval is dependent on the errors of all previous subintervals.

Given the unsatisfying result for the full theory, we will in the following section discuss

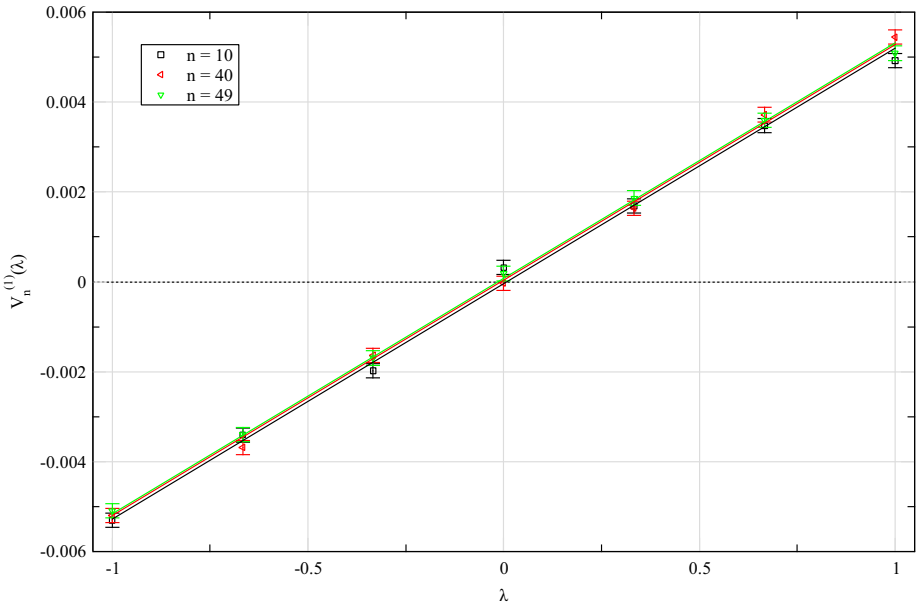

Fig. 8: Results for the normalized restricted expectation values plotted over the parameter λ. The lines depict the linear fits of the data in the same color. The Monte Carlo simulation was performed on a 4×4 lattice with $N = 100$ Chebyshev factors, a fermion mass of $m = 1$ and a gauge coupling of $\beta = 6$.

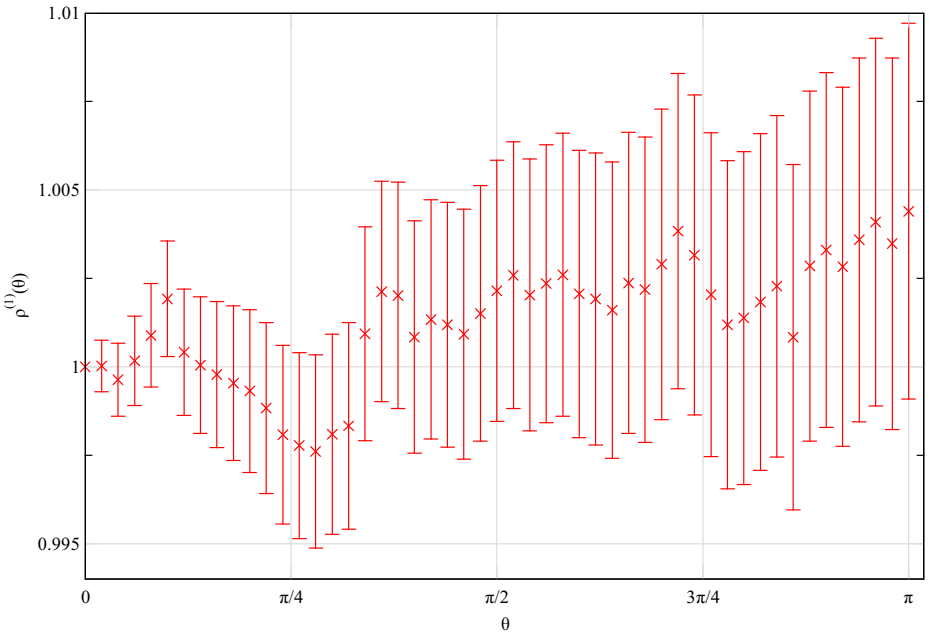

Fig. 9: Results for the Monte Carlo simulation of the density of states $\rho^{(\mathbb{1})}(\theta)$ for the full theory. The Monte Carlo simulation was performed on a 4×4 lattice with $N = 100$ Chebyshev factors, a fermion mass of $m = 1$ and a gauge coupling of $\beta = 6$.

additional steps we took to review the results obtained above to ensure they are correct and how they might be improved. Firstly, to check our code for programming errors, we used the implementation of the full theory to obtain results of the free theory, which can be compared with analytic results. Secondly, we also verified that our Monte Carlo implementation of the theory is gauge invariant. This is of course a central property of gauge theories like QCD. Thirdly, we examine the behavior of the simulation under a particular discrete symmetry, called the center symmetry of SU(3), which is given by a Z_3 rotation of specific gauge links. Finally, we will also introduce a different fitting procedure to obtain the density. This method will give much smoother results, since it is a global fit, using all subintervals and λ values at the same time and does not rely on a piecewise linear function.

7.3. Error Discussion and Possible Improvements

7.3.1. Free Theory With Six Species of Fermions

Since the results in Fig. 9 look rather chaotic and do not seem to represent physical properties, the question arises if the problem is just some accidental coding error. In this and the next section we discuss tests we performed to ensure that this is not the reason for the results we obtained.

First of all, when considering a simple programming error, it is helpful to keep in mind that we already know that the implementation of the free theory yields correct results. This of course suggests that, if an error exists, it could only have emerged during the introduction of the SU(3) structure. To verify that no mistake was made, we can use the code for the full theory to calculate an observable of the free theory, which is independent of the gauge links.

An obvious way to achieve this is by setting all gauge links equal to unity, $U_\nu(n) = \mathbb{1}$, $\forall \nu, n$, and to not perform any Monte Carlo updates for the links in the simulation. This way the different color entries of the pseudofermions never interact with one another. Therefore this describes a free theory, because now the three colors behave like non-interacting flavors. Since we implemented the squared Dirac determinant in the full theory, this means that the code now simulates six non-interacting, mass degenerate quarks. As before, such a free theory can be solved analytically using the Fourier transform of the Dirac operator. In this case now, the result is simply given by taking the sixth power on the right hand side of Eq. (66). This enables us to verify the numerical results.

For the implementation we did not use the analytic results for the slopes $k_n^{(\mathbb{1})}$ to position the λ values as we did for the free theory in Section 6.2, but just centered them around zero. Also, we chose the interval to be larger and distributed the λ values evenly within

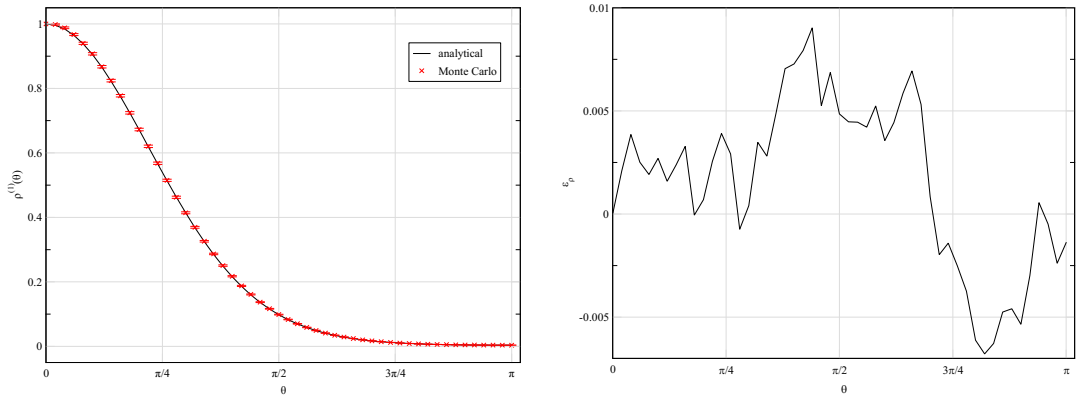

Fig. 10: Results for the Monte Carlo simulation of the density of states $\rho^{(\mathbf{1})}(\theta)$ for six non-interacting quarks using the code for the full theory. On the left-hand side, the comparison to the analytic solution can be seen, and on the right the relative error ε_ρ is plotted.

$[-5, 5]$. The mass of the fermion was set to $m = 0.5$ and the number of measurements performed were $n_{meas} = 10^6$. All other parameters are the same as in the full theory described in Section 7.2.

The results for this calculation can be seen on the left in Fig. 10, where also the analytic solution is plotted. On the right, the relative error, calculated via Eq. (71), is shown. These results clearly show that the implementation of the additional matrix structure did not lead to the introduction of a programming error, since they agree very well with the analytic solution. In fact, compared to Fig. 7, the results are even better. This can only be explained by the fact that different λ values were used in the calculation, which also yielded a very different behavior of the relative error. Except for the part of the code that performs the gauge link update, these results rule out the possibility of a simple coding error.

7.3.2. Local Gauge Invariance

In this section, we use another strong test to find possible errors in our code. Here, we check whether the implementation is invariant under local gauge transformations. This is a central property of gauge theories. We will, however, not go into much detail about this crucial element of the theory, but only state the important facts needed for the discussion in this short section. For a detailed description we refer to the literature.

Local gauge invariance tells us that at every position in spacetime the fermion fields can be transformed in such a way that the theory is left invariant. This invariance means that the action, and therefore also the Monte Carlo simulation, do not change. This fundamental property necessitates the interaction between the fermionic matter

fields and the gauge fields [3], or in our lattice description, the interaction between the pseudofermions and the SU(3) gauge links.

On the lattice, these gauge transformations can be written in the following way [2]:

$$\begin{aligned} \boldsymbol{\phi}(n) &\to \boldsymbol{\phi}'(n) = \Omega(n)\boldsymbol{\phi}(n), \\ U_\nu(n) &\to U'_\nu(n) = \Omega(n)U_\nu(n)\Omega^\dagger(n+\hat{\nu}). \end{aligned} \tag{77}$$

Every pseudofermion field on every lattice site can be multiplied with a random SU(3) matrix $\Omega(n)$, which can be different for every site. To guarantee invariance of the theory, the gauge links are defined to transform via the two transformations of the neighboring matter fields which the link connects. With these transformation properties it is straightforward to show analytically that all parts of the action in Eq. (74) are invariant.

To test if this invariance is also given in the numerical implementation, we calculated the Metropolis weight given in Eq. (A.8) twice for every update. At first, we evaluated it normally as given in the appendix, but before we calculated it a second time, we performed the gauge transformations of Eq. (77) with randomly generated SU(3) matrices Ω. For a correct implementation of the theory, these two versions of the Metropolis weight have to be equivalent. This is what we found for our implementation, which means that the important gauge invariance is preserved in our code. This fact, together with the results shown in Fig. 10, gives a strong indication that other factors besides a coding error are responsible for the unsatisfying results of the density.

7.3.3. Z_3 Update of the Gauge Links

In this section we present another possibility we considered to help improve our results for the full theory. For this, we introduce an additional update for the gauge links which uses elements of the center of the SU(3) group. The update consists of multiplying all gauge links in a random time slice of the lattice which point in time direction with a random center element, which are given by

$$Z = e^{i\frac{2\pi n}{3}}\mathbb{1}, \quad n \in \{0,1,2\}\,. \tag{78}$$

This update corresponds to a discrete symmetry, which is only present in the pure gauge theroy, called the Z_3 *symmetry* or the *center symmetry*. Using the defining property of the center elements, namely the fact that they commute with all elements of the group, it is easy to verify that the gauge part of the theory, the gauge action of Eq. (10), is invariant under such transformations. If the gauge fields interact with matter fields, however, this symmetry is broken explicitly. Nonetheless, this Z_3 update still poses a valid offer for the change of the gauge fields in the Monte Carlo simulation.

Due to the unsatisfying results seen in Fig. 9, this update procedure was implemented

with the intent to help the gauge links to easier reach all possible configurations. Also, the implementation of this update is very simple at this point, since it is just a slightly modified gauge link update, which was of course already part of the simulation.

With this additional update implemented, we performed short test runs to compare the behavior of the simulation with and without this Z_3 transformation. As it turns out, the additional updates do not have an effect at all, due to the fact that they are always rejected. This was of course anticipated as a possible behavior of the simulation. The Z_3 update is, after all, a non-local and parameterless transformation, which means there is no possibility to control the magnitude of the variation. This is of course in contrast to all other implemented updates, all of which have a variable parameter δ.

Summarizing the last three sections, we can say that we are confident that a coding error is not the culprit for the unsatisfying results and that the problem has to lie somewhere else. A possible weak point may be the simple gauge link update in our Monte Carlo simulation. Therefore, we implemented the additional Z_3 update to help the gauge links to find their way through configuration space, but unfortunately to no avail. A possible way forward from here would be to try brute force and aim at a better result by increasing the number of measurements, but that would demand much computer time. Therefore, the best option would be to implement more sophisticated gauge link updates in the Monte Carlo simulation, for example the *Heat Bath* or the *Hybrid Monte Carlo* algorithm [2].

7.3.4. Global Fit

Finally, in this last section, we want to discuss a fitting method which can be used to smoothen out some fluctuations of the density. For our specific case this might not be of much help, but it opens up very interesting possibilities for future applications.

The reason why fluctuations can arise is because $\rho^{(\mathbb{1})}$ is not given by one continuous function, but instead is just piecewise linear due to the definition of L in Eq. (30). For the results in Fig. 9, the measurements in every subinterval I_n were fitted separately to get the slope of the density for that interval. These results were then put together via Eq. (31) to obtain the piecewise linear approximation. To avoid this, it is possible to use a different fitting procedure for the restricted expectation values which fits all subintervals simultaneously and yields much smoother results.

For this global fit we can make use of the fact that for $\mathcal{J} = \mathbb{1}$ the density is an even function, as shown in Appendix A.1. This of course means that the function L is also even and we can therefore write it as a simple polynomial of the form

$$L(\theta) = \sum_{\ell \in \{2,4,\ldots\}} a_\ell \theta^\ell, \tag{79}$$

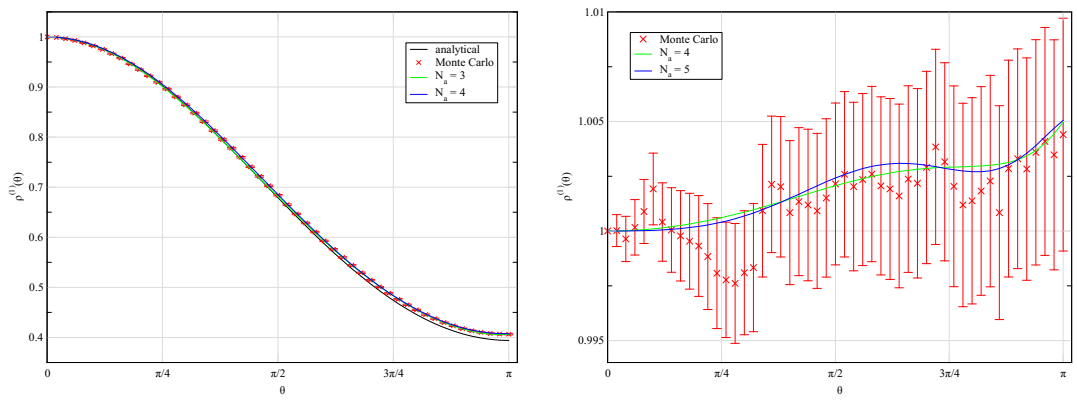

Fig. 11: Plot of the global fit compared to the piecewise linear approximation of the density $\rho^{(\mathbb{1})}$, where N_a denotes the number of coefficients used in the fit. The results on the left hand side show free case from Fig. 7, and the one on the right the full theory from Fig. 9.

where the number of terms can be varied to yield the best result for the fit. From the piecewise function Eq. (31) it is easy to see that $L'(\theta) = k_n^{(\mathbb{1})}$, with $\theta \in I_n$. For the continuous function, therefore, we can demand that the slope in the middle of the n-th subinterval is equal to $k_n^{(\mathbb{1})}$. To express the middle of this interval we can write $\sum_{i=0}^{n-1} \Delta_i + \frac{\Delta_n}{2} = \frac{2n+1}{2}\Delta$, where for the right hand side we used the fact that in our calculation all subintervals are of the same size, $\Delta_n = \Delta$, $\forall n$. This then yields

$$L'\left(\frac{2n+1}{2}\Delta\right) = k_n^{(\mathbb{1})}. \tag{80}$$

The expression in Eq. (80) can then be inserted for the slope in the linearized function $\widetilde{h}$ of Eq. (70). The fitting parameters for the global fit are then the coefficients a_ℓ.

For our tests of this fitting procedure, we implemented the very simple *gradient descent* method of the form

$$\mathbf{a}^{(t+1)} = \mathbf{a}^{(t)} - \gamma \operatorname{grad} F(\mathbf{a})\Big|_{\mathbf{a}=\mathbf{a}^{(t)}}, \tag{81}$$

where $\mathbf{a}$ denotes a vector containing the fitting parameters, F is the function dependent on the parameters that needs to be minimized, t counts the number of iterations and the parameter γ controls the step size in the direction of steepest descent. Since we are using the linearized function for the fit, γ can be calculated explicitly. The results we obtained using this method are shown in Fig. 11.

As can be seen, the results of the free theory can be fitted very nicely with only three or four coefficients in the polynomial of Eq. (79). For the full theory, however, due to the chaotic results, more parameters are needed to obtain a reasonable fit, which makes the convergence of this fitting procedure much slower. Still, it is clear that with this

fitting method smaller variations in the density can be smoothed out. Since we only wanted to discuss the general idea of this global fit, we did not concern ourselves with calculating the corresponding error bars. This can here also be done via the Jackknife method, although it is more involved for this case than it is for the piecewise linear fit.

An advantage of this fitting procedure can also be seen when remembering that, in order to calculate observables with this density of states method, one still needs to evaluate the integration of Eq. (27). For this integral, which also includes an oscillatory Fourier factor, a detailed expression for the density is needed. Here it is therefore also an advantage if a smooth polynomial expression for ρ is available.

Finally, we also want to mention that the gradient descent method is a very simple fitting procedure. Thus, despite the fact that it yields good results in our tests, it might be necessary, especially for general observables $\mathcal{O}$, to use more sophisticated algorithms, for example *conjugate gradient* methods. For detailed descriptions and examples of these methods the reader is referred to [19].

8. Summary and Outlook

In this thesis we investigated the behavior of the strong interaction for finite densities by using a lattice regularized formulation of QCD in 2 dimensions. This description of the theory is affected by the so-called complex action problem, which prohibits the use of straightforward Monte Carlo simulations. The goal of this work was to test and study a numerical technique called the canonical density of states approach. Rewritten in terms of this density, the complex action problem is absent and observables can again be calculated using standard numerical methods. The main challenge is here to obtain a precise description of the density, for which the functional fit approach was implemented.

In the first two chapters, we gave a short overview over QCD and its lattice description, and also introduced the chemical potential and discussed how the complex action problem arises. The third chapter is a crucial section of this thesis. Here we first introduced the canonical ensemble and then defined the corresponding density of states, followed by a detailed discussion of how it can be calculated numerically using standard Monte Carlo methods and the fitting procedure of the FFA. All following chapters then dealt with the numerical implementation of the density of states method described in this chapter.

After setting up the general idea, we first turned our attention to a crucial element in the Monte Carlo simulation, namely the fermion determinant of the Dirac operator. To this end, in Chapter 4, we presented the Chebyshev factorization. This convenient tool enabled us to avoid time consuming calculations, like evaluating the determinant explicitly, and instead allowed us to approximate the Dirac determinant with Monte Carlo simulations using pseudofermions. We discussed in detail the applicability of this factorization for the determinant by first looking at the spectrum of the Dirac operator for the non-interacting theory, and then generalizing the idea for the full theory. We explained why the value of the mass of the fermions is a crucial parameter for the convergence of this ansatz. Following that, in Chapter 5, we tested the Chebyshev factorization and were able to show that it yields good results, see Fig. 3.

In Chapter 6 we discussed a first simple implementation of the density of states method for the non-interacting theory. Here we also mentioned several important strategies for an efficient implementation of the FFA regarding Monte Carlo updates, the fitting procedure and preconditioning. We showed that the results obtained for one flavor are very consistent, but the comparison with the analytic solution in Fig. 7 showed that there is still room for improvement. For several mass degenerate quarks the agreement with the analytic result increased, see Fig. 10.

Finally, in Chapter 7, we turned to the anticipated goal of this thesis, namely the implementation of the density of states for the full lattice QCD in 2 dimensions. Here, the results obtained in Fig. 9 are unsatisfactory. Since our code passed all consistency

checks performed in Section 7.3, we concluded that the local gauge link update used in our Monte Carlo simulation is too naive and does not provide a fast enough sampling of configuration space. Therefore, it cannot yield satisfying results for this demanding calculation.

For further progress in this topic of finite density lattice QCD using the density of states approach, the most promising idea is to use more sophisticated Monte Carlo methods for the simulation of the interaction, e.g. heat bath or hybrid Monte Carlo methods. Such improvements, together with the global fit as shown in Fig. 11, can drastically increase the quality of the results.

Additionally, there are of course also different points which are worth looking into for future applications, which we did not investigate in this thesis. For example, it is possible to test a different ansatz for the density besides approximating it with a piecewise linear function, as was done in this work. But this can alter the process of calculating the density significantly. Also, a more subtle point is a more detailed investigation of the Chebyshev factorization. Here, further improvements regarding the convergence rate may be possible when choosing the shape of the ellipse of Eq. (43) with more care. With all these possible methods for improvement in mind, we are confident that future research on this density of states method can yield promising results.

A. Appendix

A.1. Symmetry of $\rho^{(\mathbb{1})}(\theta)$ under Charge Conjugation

As mentioned in Chapter 3 of this thesis, it is always possible to classify the density of states $\rho^{(\mathcal{J})}(\theta)$ from Eq. (26) as either an even an or an odd function. The exact classification is of course dependent on the observable $\mathcal{J}$ and can be checked with the help of suitable symmetry transformations. Knowledge of these symmetries can cut the numerical cost of evaluating the density in half. In this appendix we will show that the density $\rho^{(\mathbb{1})}(\theta)$, which always appears in the normalization when calculating observables via Eq. (27), is an even function under charge conjugation $\mathcal{C}$.

The effect that charge conjugation has on a system is the transformation of particles into antiparticles and vice versa. Since we are looking at the density of states of Eq. (27), we only need to consider the transformation properties of the gluons, since the fermion degrees of freedom are already integrated out and their transformation properties are reflected in symmetries of the fermion determinant. For the gauge links, the charge conjugation is given by [2]

$$U_\nu(n) \xrightarrow{\mathcal{C}} U'_\nu(n) = U^*_\nu(n) = \left(U^\dagger_\nu(n)\right)^T,$$

where the asterisk denotes complex conjugation.

To see how the density of states behaves under those transformations we need to look at the transformation properties of all the components in the integral. Since the path integral measure consists of products of Haar measures, as given in Eq. (9), it is invariant per definition, so $\int \mathcal{D}[U'] = \int \mathcal{D}[U]$. Also, the invariance of the Wilson gauge action $S_G[U'] = S_G[U]$ is easy to show with Eq. (10), since here only the real part of the plaquettes contribute. To see the behavior of the Dirac determinant under this transformation, however, we need to introduce the charge conjugation matrix C. This matrix acts only on the Dirac space and is defined by the property

$$C\gamma_\nu C^{-1} = -\gamma_\nu^T, \quad \nu \in \{1, 2\}.$$

For our choice of the γ-matrices it can be checked that charge conjugation matrix is given by $C = \gamma_1$. For the Dirac determinant we then can use C to show

$$\begin{aligned} \det D\left[U', \mu\right] &= \det\left(CD\left[U', \mu\right]C^{-1}\right) \\ &= \det\left(D\left[U, -\mu\right]^T\right), \end{aligned}$$

which can be verified using Eq. (14) and Eq. (21). Here, the transposition does of course not change the value of the determinant and can be omitted.

With this we have now all the ingredients we need to verify the symmetry of $\rho^{(\mathbb{1})}(\theta)$. Using Eq. (26) we can write

$$\begin{aligned}
\rho^{(\mathbb{1})}(-\theta) &= \int \mathcal{D}[U]\, e^{-S_G[U]} \det{}^2 D\,[U,\mu]\,\Big|_{\mu=-\frac{i\theta}{\beta}} \\
&= \int \mathcal{D}\big[U'\big]\, e^{-S_G[U']} \det{}^2 D\,\big[U',\mu\big]\,\Big|_{\mu=-\frac{i\theta}{\beta}} \\
&= \int \mathcal{D}[U]\, e^{-S_G[U]} \det{}^2 D\,[U,-\mu]\,\Big|_{\mu=-\frac{i\theta}{\beta}} \\
&= \rho^{(\mathbb{1})}(\theta). \qquad \text{(A.1)}
\end{aligned}$$

For the second line we just substituted all the gauge links with their charge conjugated counterparts, and for the third line we used all previously established properties which in turn enable us to cancel out the minus sign for the chemical potential in the last step.

This shows that the density $\rho^{(\mathbb{1})}(\theta)$ is even and only needs to be evaluated for positive values of θ. The same calculation can also be repeated for general observables $\mathcal{J}[U,\mu]$, where the symmetry of $\rho^{(\mathcal{J})}(\theta)$ is then dependent only on the transformation properties of the observables under charge conjugation.

A.2. Fourier Transformation of the Free Dirac Operator on the Lattice

The goal of this appendix is to calculate the Fourier transformation of the Dirac operator on the lattice. This can be done analytically only in the free case of the operator, which means that the link variables between the (pseudo-)fermion fields on neighboring lattice sites are set to $U_\nu(n) = \mathbb{1}, \forall\, \nu, n$. So in this appendix we work with the operator of the form Eq. (14), where the hopping matrix H is given by Eq. (51) since the gauge links are absent. Also, we are only interested in the case of an imaginary chemical potential $\mu = \frac{i\theta}{\beta}$.

In order to perform the Fourier transformation, we have to introduce the unitary matrices

$$U(n,p) = \frac{1}{\sqrt{V}} e^{in\cdot p},$$

where the volume of the lattice is given by $V = N_1 N_2$ and the dot in the exponent denotes the scalar product. Here, $p^T = (p_1, p_2)$ describes the discretized momentum on the lattice where the components are given by

$$p_\nu = \frac{2\pi}{N_\nu}\left(k_\nu + \delta_{\nu,2}\frac{1}{2}\right), \quad k_\nu = 0, \ldots, N_\nu - 1, \quad \nu \in \{1,2\}\,. \tag{A.2}$$

The term with the Dirac delta in Eq. (A.2) controls the boundary conditions we initially imposed on the Grassmann fields. For $\nu = 1$ the boundaries are periodic, but for the temporal direction, $\nu = 2$, the additional term generates anti-periodic boundary conditions.

The Fourier transform of the free Dirac operator is then defined by

$$\begin{aligned}
\widetilde{D}\,(p|q) &= \sum_{n,m\in\Lambda} U^\dagger(n,p) D(n|m) U(m,q) \\
&= \frac{1}{V}\sum_{n\in\Lambda} e^{-i(p-q)n}\left(\mathbb{1} - \kappa\sum_{\nu=1}^{2}\left\{[\mathbb{1}-\gamma_\nu]\, e^{i\left(q_\nu + \frac{\theta}{\beta}\delta_{\nu,2}\right)} + [\mathbb{1}+\gamma_\nu]\, e^{-i\left(q_\nu+\frac{\theta}{\beta}\delta_{\nu,2}\right)}\right\}\right) \\
&= \delta(p-q)\widetilde{D}'(p),
\end{aligned} \tag{A.3}$$

where for the second line we have summed over m. For the third line we have defined the two by two matrix $\widetilde{D}'(p)$, which depends only on one discretized momentum, and we used the definition of the delta function on the lattice $\delta(p-q) = \frac{1}{V}\sum_{n\in\Lambda} e^{-i(p-q)n}$. It can be seen that the Fourier transformed free Dirac operator $\widetilde{D}\,(p|q)$ is diagonal in the momentum space, due to this delta function.

Also, it is possible to express the matrices $\widetilde{D}'(p)$ on the diagonal of $\widetilde{D}\,(p|q)$ with the

help of trigonometric functions in the form

$$\widetilde{D}'(p) = \mathbb{1} - 2\kappa \sum_{\nu=1}^{2} \left\{ \mathbb{1} \cos\left(p_\nu + \frac{\theta}{\beta}\delta_{\nu,2} \right) - i\gamma_\nu \sin\left(p_\nu + \frac{\theta}{\beta}\delta_{\nu,2} \right) \right\}, \tag{A.4}$$

where it is also often convenient to absorb the chemical potential into the definition of the momentum via

$$p_2' = p_2 + \frac{\theta}{\beta}. \tag{A.5}$$

A.3. General Structure of Monte Carlo Simulations

In the main text of the thesis there are three instances where we employ Monte Carlo simulations which all have the same overall structure. Therefore, in this appendix, we discuss the procedure in general terms which is then applicable for all three cases. The exact details for each application are of course discussed in the main text.

What all of our simulations have in common is that we want to calculate some observable $\mathcal{O}$ via a path integral as it is shown in Eq. (3). In order to do that we need to generate field configurations which follow a distribution given by a weighted Boltzmann factor of the form $\frac{e^{-S}}{Z}$, where S is the action and Z the partition function of the theory of interest. In general, we have integrations over scalar variables as well as integrations over different fields. The fields usually have several components which are denoted by indices. In this general discussion, we will represent this fact with the notation χ_σ, where χ can be substituted for any field or variable and σ is a multi-index which combines all indices of the quantity of interest.

The structure of the Monte Carlo simulations can be summarized in the following steps, which are also derived and explained in [2], for example.

1. **Initialization:** The first step is to choose an initial configuration of the fields. We will implement this by setting all χ_σ to some fixed starting value. This is called a *cold start*.

2. **Sweeps:** To generate configurations of the fields with the desired distribution, propose a small random variation for one field component with index $\sigma = \sigma_0$. This update can be expressed via

$$\chi_{\sigma_0} \to \chi'_{\sigma_0}. \tag{A.6}$$

   For some variables it needs to be checked if χ'_{σ_0} still lies within the allowed bounds of the variable. If it does not, the proposed change is discarded immediately. Otherwise, if χ'_{σ_0} is a valid value, the change of the action under this variation is calculated by

$$\Delta S = S[\chi_\sigma]\Big|_{\chi_{\sigma_0}=\chi'_{\sigma_0}} - S[\chi_\sigma]. \tag{A.7}$$

   To check if this change in the configuration is accepted, calculate a random number $r \in [0, 1)$ and the Metropolis weight

$$\rho = e^{-\Delta S}. \tag{A.8}$$

   Accept the offer χ'_{σ_0} as the new value for this field if the condition $r < \rho$ holds. Otherwise reject the proposed update, which means that the value of the field at $\sigma = \sigma_0$ does not change. This procedure has to be repeated for all indices in σ and

also for all variables χ. This is called a sweep. There are two variants of how such sweeps are used.

a) **Equilibration:** In the beginning of the simulation a given amount of initial sweeps are performed. This is done to update the system into an equilibrium distribution which is independent of the starting configuration. The number of these equilibration sweeps is called n_{equi}.

b) **Measurements:** After the system has reached equilibrium, the observable $\mathcal{O}[\chi_\sigma]$ can be calculated using the configurations generated by the algorithm. The evaluation of the observable from a single configuration is called measurement. Single measurements are always separated by n_{skip} update sweeps. This procedure, called decorrelation, ensures that the configurations for the measurements are sufficiently different. The total number of measurements that are taken is called n_{meas} and all of these results are saved into a file.

3. **Processing the data:** The last step of the Monte Carlo simulation is to evaluate the data. Hereby the mean of the data set is calculated to obtain an expectation value of the observable via

$$\overline{\mathcal{O}} = \frac{1}{n_{meas}} \sum_{i=1}^{n_{meas}} \mathcal{O}_i, \tag{A.9}$$

where $\mathcal{O}_i$ denotes the i-th measurement of the observable. Obtaining a reasonable expression for the statistical error is not so simple, however. Despite the fact that we use n_{skip} decorrelation sweeps the obtained data set does not consist of independent measurements. This has to be taken into account when calculating the statistical error. How this can be achieved is discussed below.

These steps are universal to all our Monte Carlo applications. We also want to go into a little more detail about the update procedure in Eq. (A.6). Here it is desired to propose a configuration which is "in the neighborhood" of the old one, which means that the random variation should be reasonably small. A measure to check if this condition is true is the acceptance rate of these proposed variations, which should neither be too high nor too low. If the acceptance is too low, for instance, a lot of computer time is used without actually updating the configuration. This happens if the change in the action is large. An acceptance rate which is too high, on the other hand, implies that the proposed changes of the field are very small. This implies that a lot of sweeps would be necessary for equilibration and decorrelation, since the configurations of the fields only vary very slowly. Therefore, for many applications it is convenient to adjust the random changes such that the acceptance rate lies approximately between 0.3 and 0.7.

Additionally, what we also want to mention here, is the fact that the main numerical effort of our simulations is the evaluation of the change in action as given in Eq. (A.7). A lot of computer time can be saved at this point, however, if we take into account that the changes of most of the fields are local. This means that most of the terms that appear in the action S cancel out when calculating the difference. Therefore we need not calculate the full action of the theory when evaluating the Metropolis weight Eq. (A.8) but only a small subset. This reduces the numerical cost of these calculations drastically. Examples of these are discussed in the main text when we talk about specific applications.

Finally, we also need to discuss how we calculate the estimate for the statistical error in the Monte Carlo simulations. Since our data are correlated, we employ a combination of data blocking together with the Jackknife method. A more detailed description of the behavior and applicability of these methods is given for example in [2] and [20].

If we have a set of N measurements of the observable $\mathcal{O}$, the first step is to separate the data into k blocks containing n elements each, so that $N = kn$. With this division of the data set we can now calculate the averages $\overline{\mathcal{O}}_i$, $i = 1, \ldots, k$, in the same way as in Eq. (A.9), only that all the elements of the i-th block are left out. This allows us to calculate an estimate for the standard deviation of the mean of the observable $\overline{\mathcal{O}}$ via

$$\sigma = \sqrt{\frac{k-1}{k} \sum_{i=1}^{k} \left(\overline{\mathcal{O}}_i - \overline{\mathcal{O}}\right)^2}. \tag{A.10}$$

It is of course necessary to find an appropriate size of blocks for this estimate. To do this, we start with a low value of n and increase this value while comparing the results for the error estimation. In general, the error first grows with n and an appropriate size of the blocks is found when the error starts to plateau. An example of this can be seen in the main text in Fig. 4.

Aside from being able to get an error estimate for correlated data, the Jackknife method is also very useful for observables which are obtained after fitting procedures. The reason for this is that the blocked data sets are still large enough so that fits can be performed. This means that it is also possible to obtain the quantities $\overline{\mathcal{O}}_i$ as the results of fits, where the error estimation can then still be calculated via Eq. (A.10). Therefore, with this method, one circumvents the need for calculating the error propagation through the fitting procedure, but it requires several fits to be performed. This is used in this thesis for all results which are obtained from calculations of the restricted expectation values.

References

[1] P. A. Zyla et al. Review of Particle Physics. *PTEP*, **2020**:083C01, 2020.

[2] C. Gattringer and C. B. Lang. *Quantum Chromodynamics on the Lattice: An Introductory Presentation*. Springer, Berlin Heidelberg, 2010.

[3] L. H. Ryder. *Quantum Field Theory*. Cambridge University Press, Cambridge, 2nd edition, 1996.

[4] K. G. Wilson. Confinement of quarks. *Phys. Rev. D*, **10**:2445, 1974.

[5] G. Bhanot, A. Gocksch, and P. Rossi. On simulating complex actions. *Phys. Lett. B*, **199**:101, 1987.

[6] J. Danzer and C. Gattringer. Winding expansion techniques for lattice QCD with chemical potential. *Phys. Rev. D*, **78**:114506, 2008.

[7] C. Gattringer and K. Langfeld. Approaches to the sign problem in lattice field theory. *Int. J. Mod. Phys. A*, **31**:1643007, 2016.

[8] A. Gocksch. Simulating Lattice QCD at Finite Density. *Phys. Rev. Lett.*, **61**:2054, 1988.

[9] M. Giuliani, C. Gattringer, and P. Törek. Developing and testing the density of states FFA method in the SU(3) spin model. *Nucl. Phys. B*, **913**:627, 2016.

[10] C. Gattringer, M. Mandl, and P. Törek. New density of states approaches to finite density lattice QCD. *Phys. Rev. D*, **100**:114517, 2019.

[11] C. Gattringer, M. Mandl, and P. Törek. New Canonical and Grand Canonical Density of States Techniques for Finite Density Lattice QCD. *Particles*, **3**:87, 2020.

[12] K. Langfeld, B. Lucini, and A. Rago. Density of States in Gauge Theories. *Phys. Rev. Lett.*, **109**:111601, 2012.

[13] D. H. Weingarten and D. N. Petcher. Monte Carlo integration for lattice gauge theories with fermions. *Phys. Lett. B*, **99**:333, 1981.

[14] M. Cè, L. Giusti, and S. Schaefer. Local factorization of the fermion determinant in lattice QCD. *Phys. Rev. D*, **95**:034503, 2017.

[15] T. A. Manteuffel. The Tchebychev Iteration for Nonsymmetric Linear Systems. *Numer. Math.*, **28**:307, 1977.

[16] C. Gattringer and I. Hip. On the spectrum of the Wilson-Dirac lattice operator in topologically non-trivial background configurations. *Nucl. Phys. B*, **536**:363, 1998.

[17] H. J. Rothe. *Lattice Gauge Theories - An Introduction*. World Scientific Publishing, Singapore, 3rd edition, 2005.

[18] M. E. Peskin and D. V. Schroeder. *An Introduction to Quantum Field Theory.* Addison-Wesley, Reading, Massachusetts, 1995.

[19] W. H. Press et al. *Numerical Recipies. The Art of Scientific Computing.* Cambridge University Press, Cambridge, 3rd edition, 2007.

[20] R. G. Miller. The Jackknife - A Review. *Biometrika*, **61**:1, 1974.